

Coronis



2017 Undergraduate Team Aircraft Design Competition

Light Business Jet Family Design





2016 – 2017 AIAA Design Competition Proposal
 Light Business Jet Family Design
 Georgia Institute of Technology

Team Members	AIAA Numbers	Signature
Daniel Wise	808961	
Avery Leonard	808867	
Katie Zhang	511449	
David Twibell	480373	
Michelle Ku	808919	
Pamir Sevincel	819687	
Thomas Rainey	593555	

Advisors:

Dr. Neil Weston

Carl Johnson

1. Table of Contents

1. Table of Contents.....	i
2. List of Figures.....	iii
3. List of Tables.....	v
4. Executive Summary.....	1
5. Proposal Requirement.....	2
6. Market Research.....	2
7. Conceptual Design.....	5
Configuration Selection.....	5
Weight Sizing.....	8
Constraint Sizing.....	11
Fuselage Configuration.....	15
Wing.....	19
Airfoil.....	20
High Lift Devices.....	22
Empennage.....	26
Propulsion.....	32
Auxiliary Power Unit (APU).....	33
8. Performance.....	33
Aerodynamics.....	33
Takeoff.....	36
Range.....	37
V-N Diagram.....	39
9. Structure and Manufacturing.....	39
Material.....	39
Wing Structure.....	41
Static Analysis.....	42
Landing Gear.....	44
10. Weight and Balance.....	46

8S Weight and Balance	46
6S Weight and Balance	51
Fuselage Manufacturing.....	53
11. Stability and Control	54
Stability Augmentation System	62
12. Subsystems.....	67
Hydraulics	67
Electric	68
Fuel	69
Pneumatic.....	70
13. Interior.....	71
Cockpit/Flight Deck Design.....	71
Cabin Design.....	72
Cabin Options	73
Economy Layout.....	73
Executive Layout	75
Utility Layout.....	75
Medical Layout	76
14. Cost and Finances	77
Eastlake Cost Estimation Model	77
Developmental Costs	78
Operational Costs.....	83
15. Aircraft Dimensions.....	86

2. List of Figures

Figure 1. Runways in the United States by length.....	3
Figure 2. In-Service Light Business Jet Takeoff Distances Compared to Passenger Count.....	4
Figure 3. In-Service Light Business Jet Takeoff Distances Compared to Max Cruise Speed.....	4
Figure 4. In-Service Light Business Jet Takeoff Distances Compared to Range.....	5
Figure 5. Possible Configuration Choices.....	6
Figure 6: Weight Regression of In-Service Light Business Jets.....	9
Figure 7: Mission Profile as Described by AIAA.....	10
Figure 8: Roskam Preliminary Design Process.....	11
Figure 9: Energy Based Constraint Sizing.....	14
Figure 10: Runway Clearance.....	15
Figure 11. Fuselage Dimensions for 6-Seater.....	17
Figure 12. Fuselage Dimensions for 8-Seater.....	17
Figure 13. Fuselage Structures for 8S and 6S.....	18
Figure 14. B737c Airfoil Section.....	21
Figure 15. Top-Down View Showing Wing Planform and Control Surfaces.....	24
Figure 16. Airfoil Section Showing Full deployments of Flaps and Leading Edge Slats.....	26
Figure 17. Geometry of the Empennage.....	31
Figure 18: Drag Polar of 8S without Pylon or Engine from CFD.....	35
Figure 19. Variation of L/D with Angle of Attack of 8S from CFD.....	36
Figure 20. Mach Number Flow Visualization around 8S.....	36
Figure 21. Eight Seater Takeoff Performance.....	37
Figure 22. 8S Payload Range Profile.....	38
Figure 23: 6S Payload Range Profile.....	38
Figure 24: 8S V-N Diagram.....	39
Figure 25. Wing Rib.....	41
Figure 26. Wing Structure Showing Rib and Spar Placement and Control Surface Cutouts.....	42
Figure 27. Wing Displacement at Maximum Load.....	43
Figure 28. Stress Distribution of Wing at Maximum Load.....	43
Figure 29. Spar and Rib Placement for FEA Analysis.....	44
Figure 30. Main Landing Gear with Oleo Shock Absorber and Trailing Link.....	45
Figure 31. Front View of Aircraft with Landing Gear Extended and Retracted.....	45
Figure 32. Isometric View of Aircraft with Landing Gear Extended and Retracted.....	46

Figure 33. Point Mass Distribution of 8S at MTOW	47
Figure 34. Top View of 8S Showing Relevant Points for Longitudinal Stability at MTOW	49
Figure 35. 8S Wing Position Constraints	50
Figure 36. Profile of 8S Center of Gravity.....	50
Figure 37. Range of Static Margin and Longitudinal Tip Over Location for 6S Given Wing Shift with 5 feet of Forward Fuselage Removed	51
Figure 38. Point Mass Distribution of 6S at MTOW	52
Figure 39. Top View of 6S Showing Relevant Points for Longitudinal Stability at MTOW	52
Figure 40. Profile of 6S Center of Gravity.....	53
Figure 41. 8S Fuselage Subassemblies	54
Figure 42. 6S Fuselage Subassemblies	54
Figure 43. AVL Lift Distribution 8S in Cruise ($C_L = 0.40$) at 41,000ft.....	56
Figure 44. AVL Lift Distribution 6S in Cruise ($C_L = 0.40$) at 41,000ft.....	56
Figure 45. Trefftz Plot for 8S in Cruise ($C_L = 0.40$) at 41,000ft.....	57
Figure 46. Trefftz Plot for 6S in Cruise ($C_L = 0.40$) at 41,000ft.....	58
Figure 47. Simulink Model for Lateral-Directional SAS.....	63
Figure 48. Simulink Model for Lateral-Directional SAS.....	65
Figure 49. Hydraulic Subsystem Schematic for 8S and 6S	68
Figure 50. Electric Subsystem Schematic for 8S and 6S	69
Figure 51. Fuel Subsystem Schematic for 8S and 6S	70
Figure 52. Pneumatic Subsystem Schematic for 8S and 6S.....	71
Figure 53. Avionics.....	72
Figure 54. Economy Layout for the Coronis 6.	74
Figure 55. Economy Layout for the Coronis 8	74
Figure 56. Executive Layout for the Coronis 8.....	75
Figure 57. Utility Layout for the Coronis 8.	76
Figure 58. Medical Layout for the Coronis 8.....	77
Figure 59. Breakdown of 8S Cost Based on Sales of 200 Aircraft over 5 Years	79
Figure 60. Minimum Selling Price of 8S over 5 Years of Production to Break Even	81
Figure 61. Aircraft Pricing Based on Sales of 200 Aircraft over 5 Years.....	82
Figure 62. Breakdown of Annual 8S Operational Costs Based on 500 Annual Flight Hours	84
Figure 63. Coronis 8S Dimensions	86
Figure 64. Coronis 6S Dimensions	87

3. List of Tables

Table I: Performance Requirements	2
Table II: Additional Requirements	2
Table III. Pugh Matrix to Determine the Most Suitable Configuration	7
Table IV: Thrust and Weight Fraction Conditions	12
Table V: Atmospheric Conditions	12
Table VI: Aircraft Conditions	13
Table VII. Design Parameters for Fuselage Sizing.....	16
Table VIII. Fuselage Component Dimensions.....	18
Table IX. Summary of Wing Parameters.....	20
Table X. Chord Lengths for the Two Wing Sections.....	20
Table XI. X-FOIL Data for the B-737c-il Airfoil.....	22
Table XII. Summary of Increase in C_{lmax} of the Wing Section due to Leading Edge Slats.....	24
Table XIII. C_{Lmax} Increment Needed from the Flaps.....	25
Table XIV. ΔCl Needed from the Flap Compared to the. ΔCl Capable from the Flap.....	26
Table XV. Class I statistical data for the empennage.	27
Table XVI. Horizontal Tail Parameters	28
Table XVII. Statistical Empennage Planform Parameters	28
Table XVIII. Empennage Planform Parameters	29
Table XIX. Vertical Tail Parameters	30
Table XX. Tail Weights.....	32
Table XXI. Specifications for the Honeywell TFE731-40AR jet engine.	33
Table XXII. Specifications for the Honeywell RE100 APU.	33
Table XXIII. Cruise condition	35
Table XXIV. Major Subassembly Weights for 8S Aircraft.....	47
Table XXV. Mass Properties of 8S Aircraft.....	48
Table XXVI. Comparison of Neutral Point Determined with Class II Methods and AVL	58
Table XXVII. Eigenvalue analysis for the longitudinal dynamics of the Coronis 6S	63
Table XXVIII. Eigenvalue analysis for the longitudinal dynamics of the Coronis 8S	63
Table XXIX. Gains used for the longitudinal SAS.....	64
Table XXX. Longitudinal modes requirements and results.....	64
Table XXXI. Eigenvalue analysis for the lateral dynamics of the Coronis 6S.....	65
Table XXXII. Eigenvalue analysis for the lateral dynamics of the Coronis 8S.....	66
Table XXXIII. Gains used for the lateral SAS.	66

Table XXXIV. Lateral-directional modes requirements and results.....	66
Table XXXV. Cabin design parameters.	73
Table XXXVI. Summary of financial decisions.	81
Table XXXVII. Summary of operational costs.	83
Table XXXVIII. Comparison of the operational cost to various aircraft of similar type.	85

4. Executive Summary

This AIAA competition requested a family of light business jets with a focus on part commonality, reliability, and minimal acquisition and operating cost. The light business jet market is saturated with dozens of aircraft that all perform similar missions with only small variations in features and performance. To successfully enter this market, there needs to be some niche within which the aircraft occupies. It was discovered that today's jets capable of carrying 6 – 8 people cannot operate out of airports with runways less than 3,000 feet. Improving takeoff performance in this regime drastically improves access to airports in the United States and differentiates this plane from the rest of the market. Many light business jet operators do not operate larger jets because they seek an excellent value aircraft that can access more domestic airports. Short takeoff performance is key to making these airplanes as versatile as possible and thereby meeting another primary design goal.

The final aircraft configuration was a standard composite fuselage with a swept low-wing and T-tail. Both the six and eight seaters were identical except for a small change in the fuselage and flight controller, resulting in 94% part-commonality by weight which minimizes the development, certification, and manufacturing costs a significant amount. Short takeoff performance was achieved with a high thrust to weight ratio and multiple high lift devices. This resulted in takeoff performance that allowed the Coronis aircraft to access 28% more airports in the United States compared to jets in the same category. Preliminary design analysis was validated with finite element analysis, computational fluid dynamics, and extended vortex-lattice models. Based on the aircraft weight, complexity, and performance, the Eastlake cost model estimates our aircraft to be priced competitively to various aircraft of similar maximum takeoff weight.

5. Proposal Requirement

The AIAA Request for Proposal (RFP) for the Light Business Jet Family Design Challenge listed the following design objectives: designing a two-family business jets (6 seater and 8 seater) with high part commonality for minimizing development and production costs, minimizing acquisition and operating costs, and entry-into service by 2020. The specific RFP requirements are listed on Table I and Table II.

Table I: Performance Requirements

MMO	0.85 at 35,000 ft
Rate of Climb	3,500 fpm
Service Ceiling	45,000 ft
Maximum Field Length	3,600 ft
NBAA IFR Range	2,500 nm

Table II: Additional Requirements

	6 Seater	8 Seater
Certification	FAR Part 23	FAR Part 25
Baggage (lb)	500	1000
Baggage Volume (ft³)	30	60
Range Requirements	1 pilot & 2 passengers	1 pilot & 4 passengers
Max number of passengers	6	8

All requirements have been superbly met, with the exception that both variants were able to be certified under Part 23 allowing for lower certification costs and more competitively priced aircraft.

6. Market Research

The light business jet market is saturated with many aircraft capable of carrying out the same type of mission. These aircraft can generally carry half a dozen people over 2,000 nm at a cost of less than \$10 million. The customers of these aircraft are more financially conscious than the mega-rich who desire the biggest, fastest, most luxurious private jets. Customers of light business jets are in the market for a substantial value aircraft that can perform the mission reliably.

Light business jet owners in the United States generally fly the aircraft domestically because they do not have the range to fly across either the Atlantic or Pacific oceans. Domestic flights spend less time, as a percentage of the block time of the flight, in cruise than a trans-oceanic flight. This means that not as much time is saved by flying on these short haul trips unless the airports for the trip are close to the operator’s actual origin and destination. Minimization of the “first and last mile” of a trip conducted by air travel can be done by accessing smaller airports which are more evenly spread out across the United States, even far away from major population centers. Short takeoff capability means greater versatility for the passengers.

The United States has 18,762 public airports as of 2014 [1]. Half of these airports have runways that are less than 3,000 ft long. Figure 1 shows the distribution of these airports by runway length. It is interesting to note that between 3,000 ft and 2,000 ft every foot of takeoff improvement can access 6 more airports in the United States. Unfortunately, today’s light business jets capable of carrying between 6 – 8 passengers cannot land on airports less than 3,000 ft.

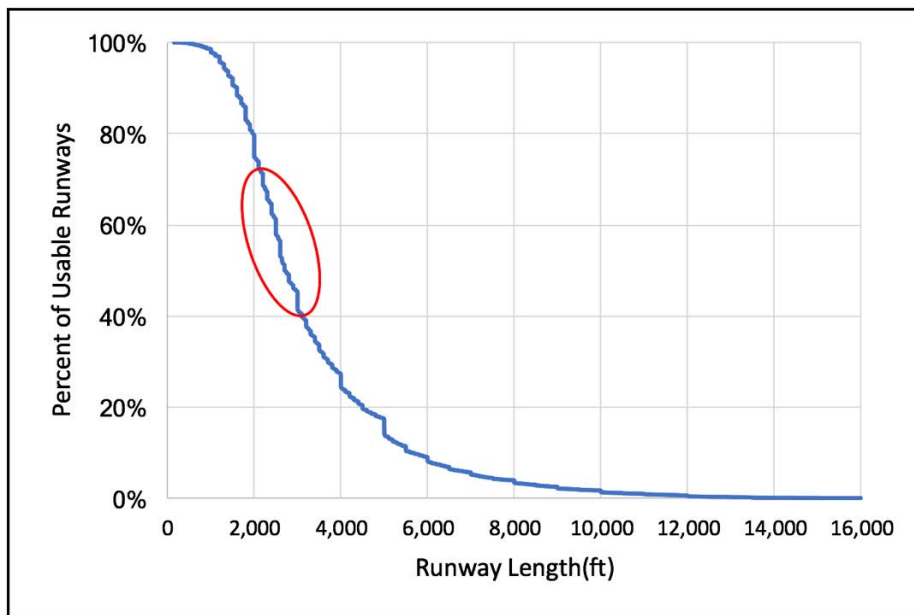


Figure 1. Runways in the United States by length

This research shows that there is a niche in the light business jet market for jets that can takeoff on runways less than 3,000 ft. Figure 2, Figure 3, and Figure 4 show that an aircraft that meets the requirements

presented in the RFP that can also takeoff from runways less than 3,000 ft will be in a totally unoccupied niche of the business jet market. This is also where the greatest improvements are made in terms of airport accessibility around the United States. Therefore, there are huge gains to be made in terms of versatility for an aircraft that can achieve the goal of operating from runways between 2,000 and 3,000 ft.

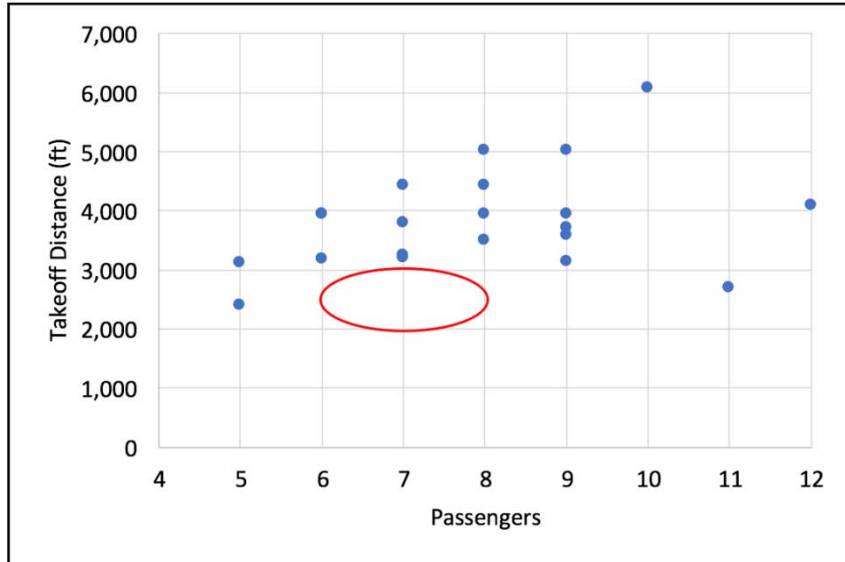


Figure 2. In-Service Light Business Jet Takeoff Distances Compared to Passenger Count

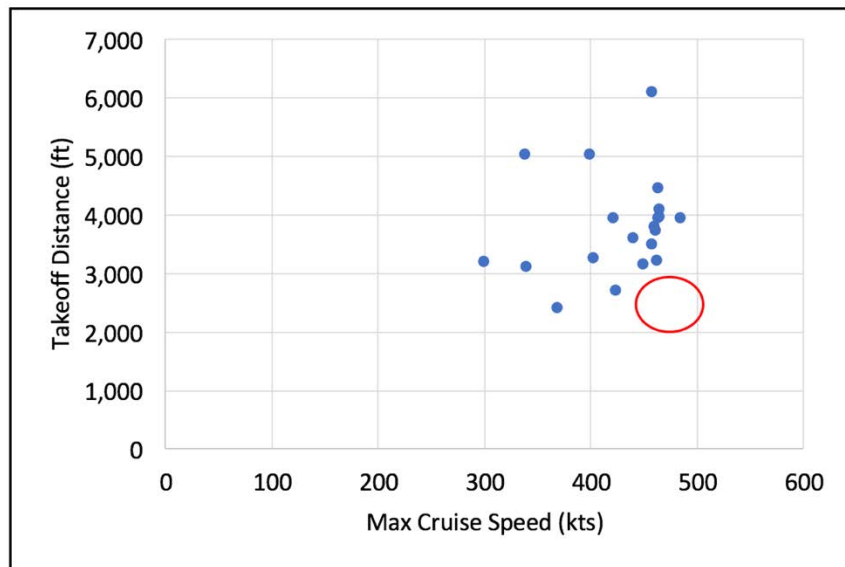


Figure 3. In-Service Light Business Jet Takeoff Distances Compared to Max Cruise Speed

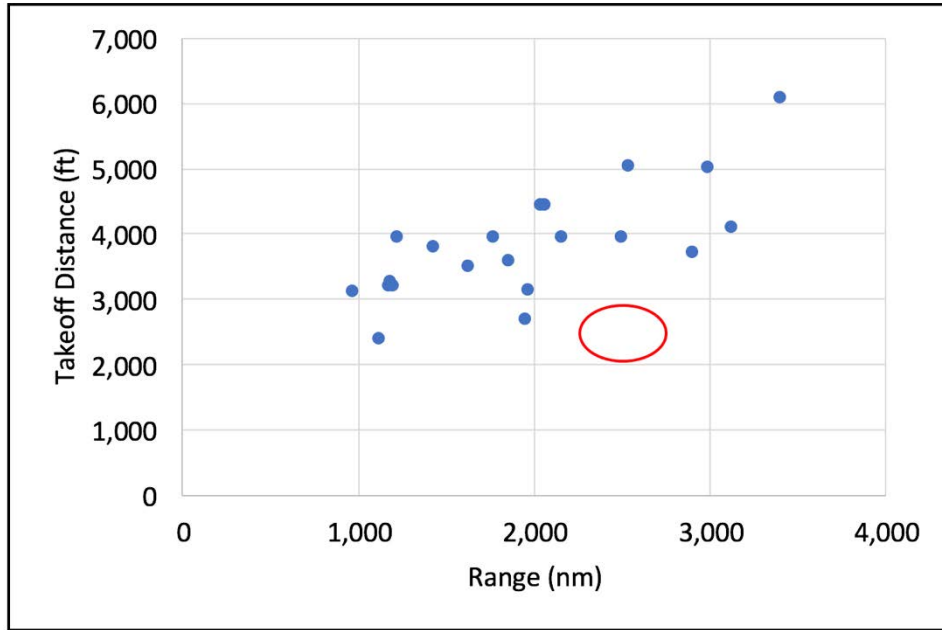


Figure 4. In-Service Light Business Jet Takeoff Distances Compared to Range

7. Conceptual Design

Configuration Selection

The configuration for the Coronis jet family was chosen after an in-depth assessment of the existing aircraft in the light business jet category. The initial configuration selection was conducted by taking into consideration the request for proposal (RFP) performance requirements and the intended future market niche. A Pugh matrix was created to evaluate each option’s strengths and weaknesses in relation to the chosen figures of merit. The figures of merit chosen were weight, manufacturability, maintenance, operating cost, aesthetics, and versatility. These were weighted based on their perceived importance to the design of the aircraft. The configuration choices considered included wing placement, landing gear, number and location of engines, and empennage arrangement. To visualize how the different configurations would look, four different designs were modeled in OpenVSP. These models can be seen in Figure 5 below.

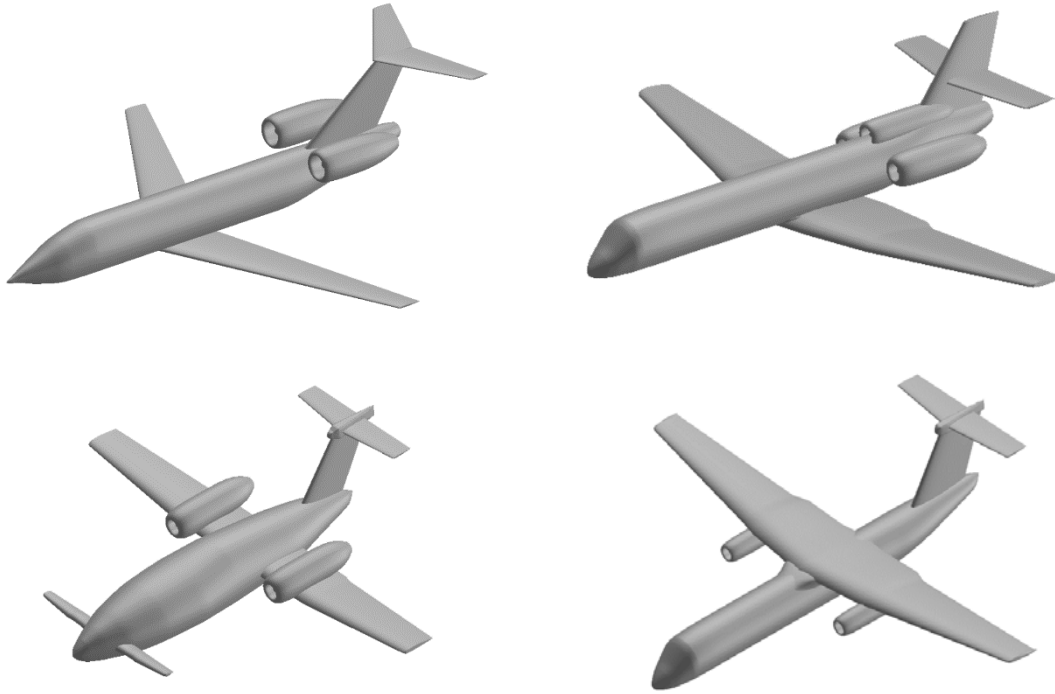


Figure 5. Possible Configuration Choices

The details of the configuration selection can be seen in Table III below. After the relevant parameters were properly weighted and options were scored, the results led to the low-wing, two-engine design shown in the upper left-hand corner of Figure 5. There were several options for the placement of the wing. A mid-wing was not suitable for our design because it would obstruct the cabin reducing the comfort of the passengers. A high-wing design would give more ground clearance if the engine were mounted on the wing and better visibility to the ground. However, the fuselage is likely too small to contain the main landing gear, meaning that the gear would need to be attached to the wing. In this case, to reach the ground, the main gear would need to be long and heavy. A canard was also considered, as it would be a unique choice for a business jet; however, the complexity would raise the overall cost of aircraft. These factors made the low-wing option the clear choice. A low wing also aids in the performance of the aircraft because of the ground effect during takeoff.

Table III. Pugh Matrix to Determine the Most Suitable Configuration

		Figures of Merit						
		Weight	Manufacturability	Maintenance	Operating Cost	Aesthetically Pleasing	Flexibility/Versatility	
	Weight Factors	25	20	15	15	15	10	
Component Category	Configuration Option	Score						Total Score
Wing	Low-Wing	5	5	5	5	5	5	5
	Mid-Wing	3	3	4	5	3	3	3.45
	High-Wing	5	4	3	5	2	3	3.85
Landing Gear	Tricycle	4	4	4	5	5	5	4.4
	Tail Dragger	5	4	4	3	3	3	3.85
Engine Location	Fuselage	5	5	3	5	5	5	4.7
	Under Wing	5	5	5	5	2	5	4.55
Number of Engines	1	5	3	5	5	2	2	3.85
	2	4	5	4	4	5	4	4.35
	3	3	3	3	3	3	5	3.2
Empennage	T-Tail	3	5	3	5	5	5	4.2
	Cruciform	4	5	3	4	3	5	4
	V-Tail	5	5	2	4	3	5	4.1
	Conventional	4	5	3	4	3	5	4
	Canard	4	2	3	4	4	3	3.35

Tail design is important for the stability of the jet. A conventional tail was considered; however, the airflow would be disturbed by the wing and engines. A V-tail would be lighter than the other choices and would also potentially produce less interference drag. However, it will require a more complex control system design since each control surface will now control both pitch and yaw (coupling effect). A T-tail was the final choice for the design as it would aid in drag reduction and keep the tail plane far away from the engine exhaust gas.

For the power-plant design, there were two decisions that had to be made – the engine placement and the number of engines. A two-engine configuration was chosen because it would provide appropriate redundancies for flights across oceans. A three-engine configuration would be costly and overly complicated. Placement of the engines under the wing was initially considered, however there were concerns for foreign object debris (FOD) and ground clearance for a low wing design. Engines that are placed high on the empennage would help lift, reduce drag, and aid in the reduction of asymmetric yaw should there be an engine failure. It would also enable a lower fuselage height which would allow the customer to quickly and efficiently board the aircraft.

Weight Sizing

Class I weight sizing was completed as described in Roskam Part I [2]. The process involved estimating aircraft characteristics, like wing loading, drag coefficients, and TSFC, which were then used to iterate through a program which was designed by the team and which followed the Roskam method. With the given estimates and inputs, the program solved for the necessary fuel fractions in every phase of flight. These fuel fractions were then used to determine the empty, maximum takeoff, and maximum fuel weights of the aircraft by applying an equation of curve fits to the weights of aircraft already in existence which were chosen for expected similarity to the Coronis design. These aircraft ranged in weight from the very light Cirrus Vision SF50 to the Gulfstream G-280. Aircraft were chosen based on having a weight which fell in a given weight class range, ideally had some amount of composite structure, and were designed and

manufactured within the last forty years. Since not all the aircraft were designed with the newest manufacturing and weight saving methods a technology factor was applied to move the weight prediction to the lighter side of the given variation in weights. This moved the design into the weight class of recently built aircraft which fall into the light to medium weight classes. Aircraft of similar weight included the Pilatus PC-24, Cessna Citation XL, and the Embraer Phenom 300.

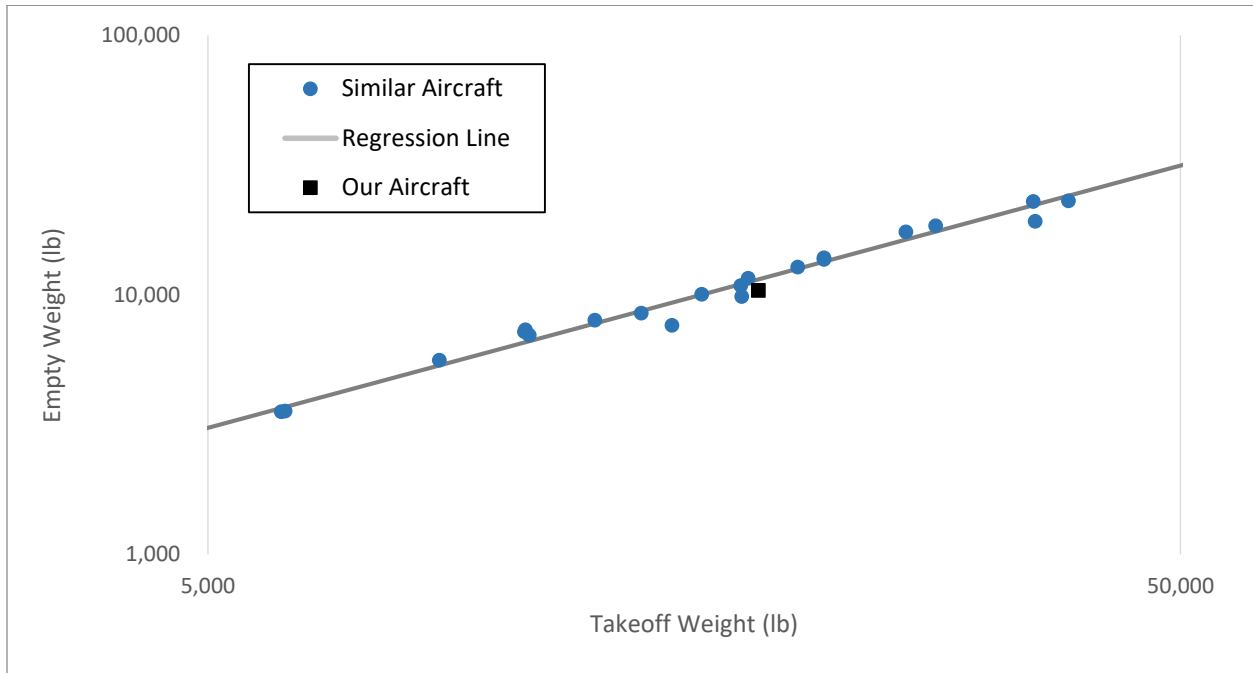


Figure 6: Weight Regression of In-Service Light Business Jets

The weight sizing was first completed for the eight-seat version, since this version must carry more baggage, cabin weight, and structural weight than the six-seat variant with the same engines over the same specified range. For the long cruise range, the aircraft must be able to have a minimum range of 2,500 nautical miles assuming an NBAA IFR range profile with a lower altitude cruise to a 100 nautical mile alternate airfield in addition to the minimum enroute range. Four passengers and one pilot were required to be carried with each weighing 200 lb. The total weight of baggage was assumed to be 250 lb (one quarter of the maximum required) for the four passengers and one pilot which is 50 lb of baggage per person.

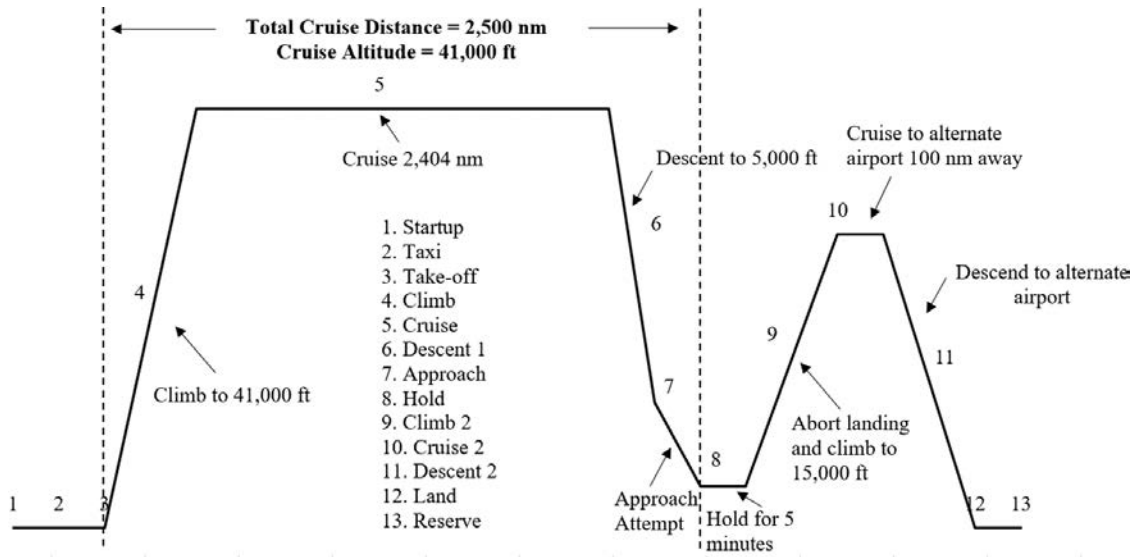


Figure 7: Mission Profile as Described by AIAA

The fuel fractions for taxi, takeoff, descent, approach, landing, and trapped oil and fuel were taken directly from Roskam Part I for business jets and are shown in Table IV. The startup fuel fraction was reduced from Roskam I value which was too conservative compared to average before takeoff fuel burn. Cruise distance was reduced for the fuel fraction calculations so that appropriate fuel weight estimates could be made for the climbs and descent where the engines are at full power and close to idle, respectively. More appropriate speeds and fuel burn rates were used during the climb and descent to accurately represent these phases of flight. Descent speed was chosen to be lower than the cruise speed at 250 knots due to expected limitations on speed below 10,000 ft MSL by ATC. Fuel fractions for endurance segments of flight, like the alternate holding time was modeled using the Breguet endurance equation with fuel fractions for cruise segments using the Breguet range equation. This cycle of weight sizing was then repeated while making small changes to the parameters which were estimated to adjust the aircraft characteristics needed to meet the mission requirements with the lowest attainable weights.

Weight sizing was run in series with the constraint sizing process with feedback to meet all the given range and point performance requirements of the aircraft. Figure 8 below shows the process flow utilized.

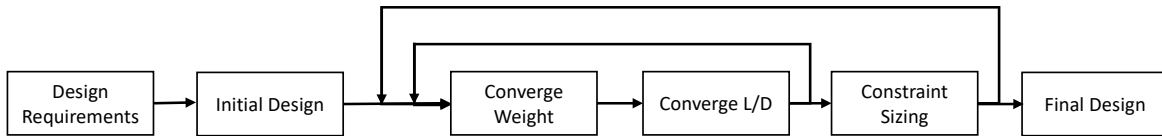


Figure 8: Roskam Preliminary Design Process

Constraint Sizing

To derive the point performance constraint sizing equations used for this project, an energy balance of an abstract aircraft model was taken with the difference in propulsive and drag forces multiplied by velocity to give the time rate of energy. The time rate of change of various inherent energies, potential energy in the form of altitude and kinetic energy in the form of speed were then set equal to this time rate of change of energy. These sets of terms were then set equal to each other to yield Equation 1.

$$(T - (D + R))V = W \frac{dh}{dt} + \frac{W}{g} \frac{d}{dt} \left(\frac{V^2}{2} \right) \quad (1)$$

This first equation was then reorganized to yield specific excess power.

$$P_s = \frac{(T - (D + R))}{W} = \frac{1}{V} \frac{d}{dt} \left(h + \frac{V^2}{2g} \right) \quad (2)$$

To simplify the above equation, instantaneous thrust and weight have been related to sea level thrust and takeoff weight through the following equations which assume that the fractions between actual thrust and sea level thrust are known as well as the actual weight from the initial takeoff weight.

$$T = \alpha T_{SL} \quad (3)$$

$$W = \beta W_{TO} \quad (4)$$

To determine the thrust fraction α a custom engine deck model was developed to account for speed, altitude, and power setting. The weight fraction β was determined by considering the fuel weight fractions already determined for the weight sizing analysis previously discussed. Making these substitutions, and solving for specific takeoff thrust then yields the following equation.

$$\frac{T_{SL}}{W_{TO}} = \frac{\beta}{\alpha} \left(\frac{(D + R)}{\beta W_{TO}} + \frac{1}{V} \frac{d}{dt} \left(h + \frac{V^2}{2g} \right) \right) \quad (5)$$

The lift equation was then considered with load factor included to account for non-inertial loads.

$$L = n\beta W_{TO} = qSC_L \quad (6)$$

The lift equation was then solved for the lift coefficient and substituted into the drag equation to yield a final specific thrust equation with all known or assumed parameters for this project which is given below in Equation 7. Note that this final form of Equation 7 was utilized for all cases except the takeoff case which will be discussed later. A complete set of variables were determined for each case and were then substituted into this general equation to yield the thrust loading as a function of wing loading. These cases are shown below in Table IV.

$$\frac{T_{SL}}{W_{TO}} = \frac{\beta}{\alpha} \left(\frac{qS}{\beta W_{TO}} \left(k \left(\frac{n\beta W_{TO}}{qS} \right)^2 + C_{D0} + \frac{R}{qS} \right) + \frac{1}{V} \frac{d}{dt} \left(h + \frac{V^2}{2g} \right) \right) \quad (7)$$

Table IV: Thrust and Weight Fraction Conditions

	Flight Condition			
	Max Speed	Max Rate of Climb	Service Ceiling	Approach
Thrust Fraction Condition	Full Power Max Speed	Full Power Best Climb Speed	Full Power Min. Cruise	Full Power Approach Speed
Thrust Fraction (α)	0.287	0.792	0.143	0.819
Weight Fraction Condition	Top of Climb	Start of Climb	Top of Climb	Approach
Weight Fraction (β)	0.887	0.988	0.887	0.696

Table V: Atmospheric Conditions

	Flight Condition			
	Max Speed	Max Rate of Climb	Service Ceiling	Approach
Altitude (ft)	35,000	0.0	45,000	0.0
Density Lapse Ratio	0.6293	1.0	0.2476	0.7619
Temp. (°R)	465.23	518.69	389.99	486.61

All properties relating to speed and the required performance for Equation 7 are given below in Table VI. Note that speeds for the maximum speed, high g turn, and approach conditions were specified by the project assignment. The maximum rate of climb forward speed was assumed to be 300 knots as this was less than the given maximum speed which must be true if the maximum speed is in steady level flight. The same logic was applied to the service ceiling forward speed. However it was increased to 350 knots since the lower density at higher altitude requires more speed to avoid stall. Note that a speed is not given for takeoff since the rotation speed does not need to be known to solve the problem as was described regarding the derivation of Equation 7. Climb rates for maximum rate of climb and service ceiling as well as the load factor for the high g turn were also specified in the RFP. Note that all Mach numbers for each condition were calculated from the flight speed and the corresponding temperatures given above in Table 2. Note that all climb rates besides those specifically assigned were assumed to be zero and that all load factors were assumed to be one as these conditions were assumed to be in non-accelerating states.

Table VI: Aircraft Conditions

	Flight Condition			
	Max Speed	Max Rate of Climb	Service Ceiling	Approach
Flight Speed (knots)	490	170	350	105
Mach Number	0.85	0.25	0.61	0.16
Climb Rate ($\frac{ft}{min}$)	0.0	3,500	100	0.0
Load Factor	1.0	1.0	1.0	1.0

All data given above in Table IV, Table V, and Table VI, were used to calculate the thrust loading to wing loading relationship which define the design space within which the aircraft, if so equipped in thrust and wing area, can achieve all constraints and performance requirements given in the RFP. The design space for this aircraft lies within the region bounded by the maximum rate of climb curve, the high g turn

curve, and the approach wing loading line. Within this space the preferred point for thrust loading and wing loading is found at the minima imposed by the maximum rate of climb curve and the high g turn curve. Note that this preferred point was not placed on the minima but instead slight above this point to account for small uncertainties within the constraint sizing parameters. The preferred point for this project is located at a thrust loading of 0.462 and a wing loading of $70.8 \left(\frac{\text{lb}}{\text{ft}^2} \right)$.

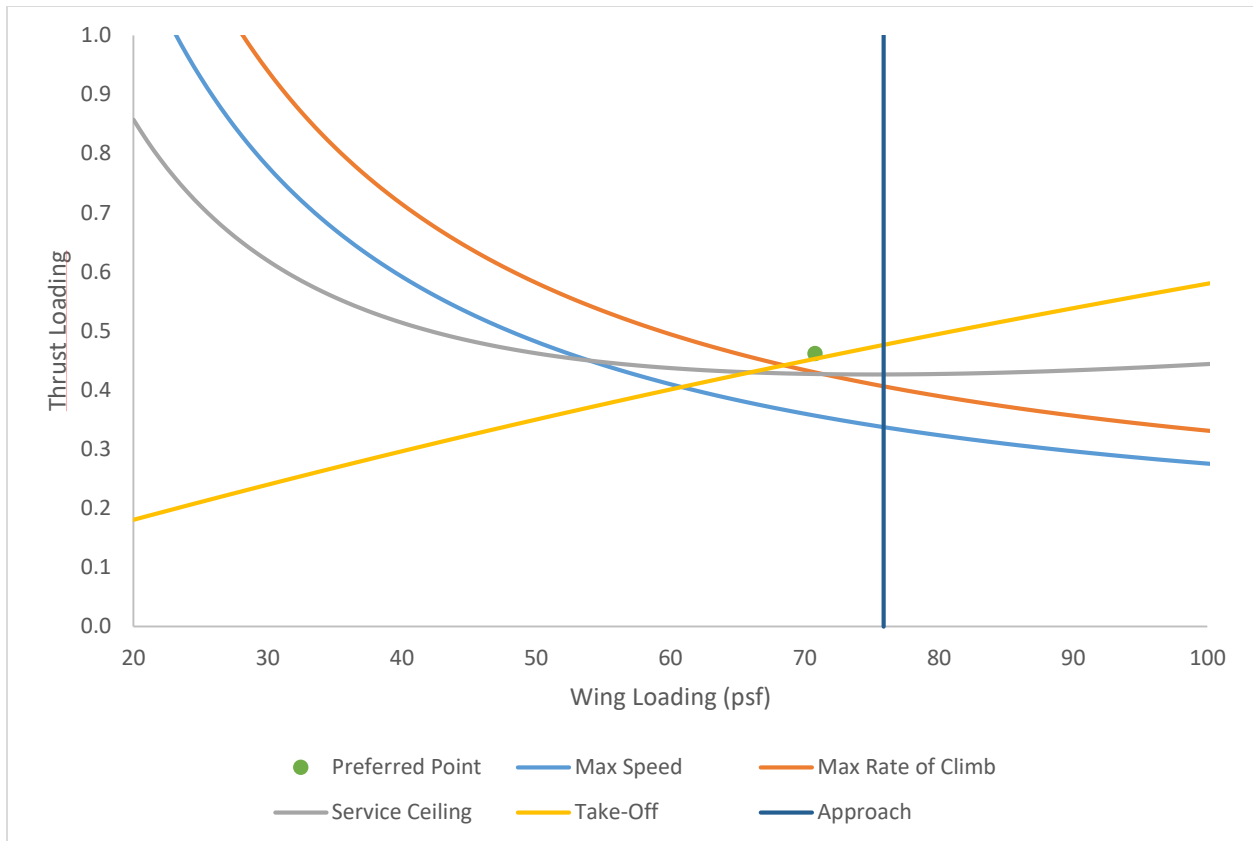


Figure 9: Energy Based Constraint Sizing

Takeoff performance was also considered in the constraint sizing process and was accomplished by means of a custom analysis written to determine the shortest capable balanced field length the aircraft was capable of at sea-level on a standard day. The takeoff analysis involved breaking the takeoff phase of flight into distinct and separate phases. Simple physics was then applied to determine the necessary distance to accomplish the phase. These phases included the accelerating ground roll, rotation, flight in ground-

effect, transition to a steady climb, followed by clearance of a 35ft obstacle in steady climb and best angle of climb speed with a graphical depiction being shown below in Figure 10.

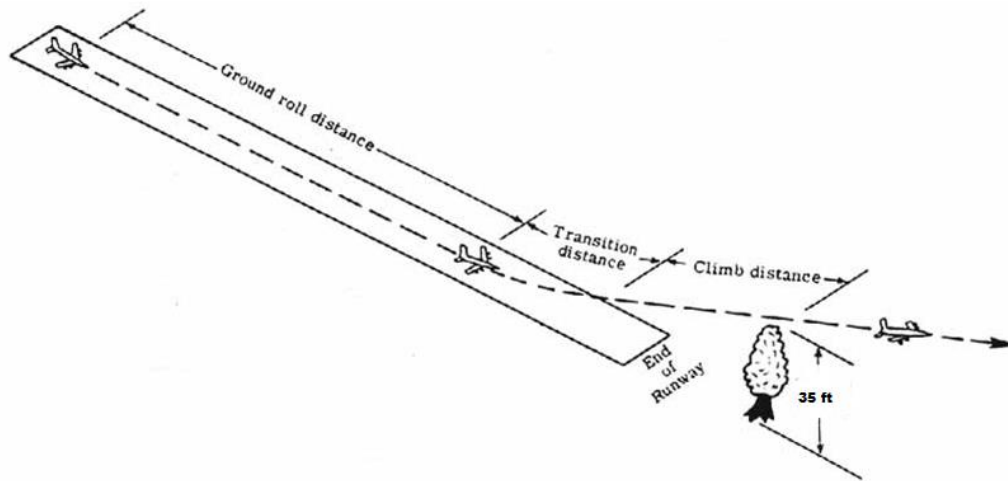


Figure 10: Runway Clearance

A Class I drag polar from Roskam was used for L/D estimation in both the weight estimation calculations and constraint sizing steps. The Oswald efficiency factor was chosen to be 0.85, because it is an average value for an efficient wing from aerodynamic theory. Aspect ratio was chosen to be a medium to high value of 9 for a business jet to achieve the L/D necessary for long-range cruise. An initial guess of the thickness to chord ratio was chosen to be 12% in that a thin airfoil was desired with still having sufficient inside volume for fuel storage. A Class II drag polar was then used to update the drag estimation after a rough picture of the aircraft had taken shape.

Fuselage Configuration

A traditional single fuselage for transport aircraft was the only type of fuselage configuration considered. There were several reasons for this design choice. From a design point, a single fuselage configuration would allow for ease of structural part commonality that was stated initially from the RFP. This would also allow for a lighter aircraft and simplicity in design, reducing manufacturing costs. From a consumer standpoint, a single fuselage would allow greater passenger comfort through spacious

accommodations. Conversations among passenger could occur across aisles that would not otherwise be possible with a multi-fuselage design.

The dimension sizing of the fuselage was conducted by analyzing data gathered of aircraft of similar missions and sizes. Roskam Part II aided in the proportionality of the length to width ratio of the design. A length of 45 feet was chosen from the 6-seater variant and a length of 50 feet was chosen for the 8-seater variant of the business jet. Several design parameters such as the fineness ratio were chosen based off Roskam Part II, Table 4.1 [3]. These chosen parameters can be seen in the table below.

Table VII. Design Parameters for Fuselage Sizing

Design parameter	Value
Fineness ratio ($\frac{l_f}{d_f}$)	8
$\frac{l_{fc}}{d_f}$	2.5
θ_{fc}°	11

A fineness ratio of 8 was chosen for both the 6-seater and 8-seater variants. From the fineness ratio, the height of the aircraft can be found. However, because of the need for part commonality, a universal height was chosen for both variants. This universal width was based off the 8-seater’s height calculations and was chosen to be 6.5 feet. A tail cone to diameter ratio of 2.5 was chosen based off of the range of values from Roskam and the length of the empennage was calculated to be 16.25 feet. The angle of the empennage was also found from Roskam Part II and was chosen to be the highest tail cone angle given in the business jet category to avoid the possibility of tail cone strikes during take-off. Tail strikes are a legitimate concern for aircraft that aim to achieve a short takeoff and landing. Though a fully circular cross section would be ideal for the fuselage design, as it is best for cabin pressurization, a cross section of two overlapping circles was chosen instead. This was chosen to increase the amount of passenger space and comfortability. With the overlapping circle design, the width of the aircraft became 6 feet. A figure of the fuselage dimensions for the 6- and 8-seater variants is shown below.

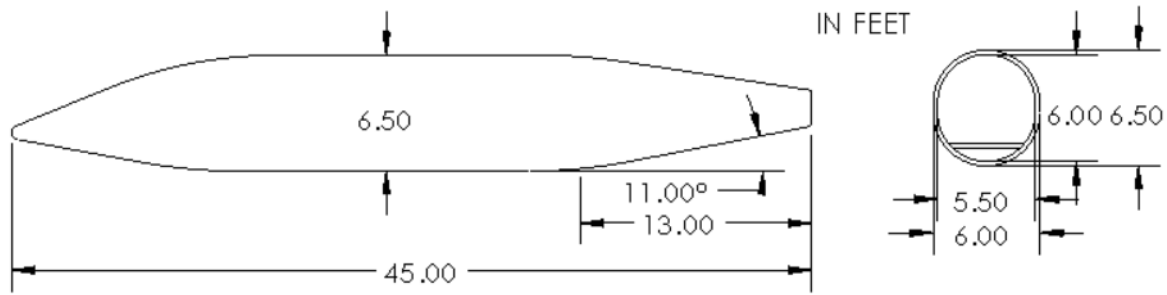


Figure 11. Fuselage Dimensions for 6-Seater

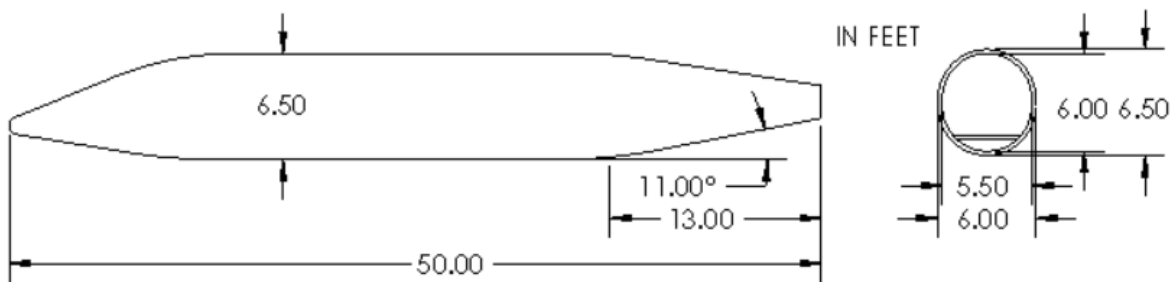


Figure 12. Fuselage Dimensions for 8-Seater

The fuselage will be manufactured from carbon fiber reinforced polymer composite material. The structure will be a semi-monocoque structure consisting of bulkheads and stringers. The stringers of the fuselage will be laid on the inside of the skin and manufactured together. These will be cured and hardened in an autoclave together. After, the windows and door pieces will be cut out. The skin thickness of the fuselage was determined to be 0.25 feet (3 inches) with the size and spacing of the stringers as 10 inches and 15 inches (1.25 feet) respectively. This was determined from the values indicated in Roskam Part III. There were several formers that were also used as structural support for the aircraft. These were spaced 1.5 feet (30 inches) apart and had a depth of 1.5 feet. One large main bulkhead was placed directly behind the cockpit and a pressure bulkhead was placed in the aft of the fuselage, before the beginning of the empennage. A general image of the structure of the 8-seater variant is shown in Figure 13.



Figure 13. Fuselage Structures for 8S and 6S

Using the conventions stated in Roskam Part III, several components of the exterior and interior of the fuselage were chosen. The floor of main cabin of the fuselage was determined to be 1 foot from the bottom of the fuselage. The window size was chosen to be 26 by 19 inches. There are three windows spaced 30 inches apart in the 6-seater variant and 4 windows spaced 30 inches apart in the 8-seater variant. From the Roskam text, main door of the fuselage was created to be 58 by 32 inches with the storage door being 47 by 34 inches. These dimensions can be seen easily in Table VIII. Fuselage Component Dimensions below.

Table VIII. Fuselage Component Dimensions

Component	Dimension
Window	26 x 19 inches
Window Spacing	30 inches
Main door	58 x 32 inches
Storage Door	47 x 34 inches

Wing

With the fuselage now sized appropriately, the wing can be designed. The wing of the aircraft is sized for the eight-seater to achieve the performance required to complete the mission. By sizing to the tougher constraints imposed by the eight-seater, the same wing will be able to be used on the lighter, six-seat variant. This will increase the commonality between the two aircraft and make the manufacturing process faster and therefore less expensive. Designing the wing includes choosing several wing parameters, selecting an airfoil, and finally designing the high lift devices. As discussed earlier in the configuration selection, the choice was made to go with a low-wing, cantilever design. The wing parameters are chosen based off similar aircraft whose data are given in Roskam Part II [3]. The aspect ratio of the wing was already chosen to be 9.0 for the aircraft sizing process with a wing area of 260 ft². From the definition of aspect ratio, the wingspan can be determined as shown in Equation (8) below.

$$b = \sqrt{AR * S} = 48.4 \text{ ft} \quad (8)$$

The root of the wing was given an incidence angle of four degrees. This made it possible for the aircraft fuselage to be approximately level while in the standard cruise condition of Mach 0.75. The wing was also given a linear twist from 4 degrees at the root down to 0 degrees at the tip. This washout ensures that the end portion of the wing where the ailerons are located will stall after the root of the wing. With the aileron portion of the wing stalling last, the pilot will be able to maintain roll control of the aircraft after the initial onset of stall. In addition to this, the washout will also help reduce the torsion on the wing near the tips. Because of the flexing that the wing naturally undergoes during flight, the region of the wing near the tips will experience a greater angle of attack than the root (which is rigidly fixed to the fuselage). By giving the wing washout, the angle of attack will decrease as the distance from the root increases. This angle of attack decrease from the twist will act to offset the angle of attack increase due to the flexing of the wing and thereby ensure that torsion near the wing tips will not exceed the structural capabilities. Because of landing gear placement constraints, the wing had to be divided into two different taper ratio sections. The first section has a taper ratio of 0.52 and the second section has a taper ratio of 0.16. This allowed for a

larger span near the root of the wing which enabled the landing gear to be placed at the proper location behind the center gravity in order to ensure the proper tip-over stability during ground operations. The wing parameters discussed above are summarized in Table IX below.

Table IX. Summary of Wing Parameters

AR	S	Wingspan	Dihedral	Root Incidence	Sweep (c/4)	Taper 1	Taper 2
9.0	260 ft ²	48.4 ft	2°	4°	30°	0.52	0.16

The chord at the root and tip of the two wing sections can be determined based off of the formula for the area of a trapezoid. This derivation yields the results shown in Equation (9) below.

$$c_r = \frac{2S}{b(\lambda + 1)} \quad (9)$$

The root chord value can be multiplied by the taper ratio for the section to find the tip chord of the section. Doing these calculations for both sections yields the following results shown in Table X below.

Table X. Chord Lengths for the Two Wing Sections

	c_r	c_t
Inboard Section	11.67 ft	6.07 ft
Outboard Section	6.07 ft	1.0 ft

Airfoil

With these fundamental wing parameters now known, the next step is to select the airfoil. Because a high-speed business jet is being designed, the first priority is to choose an airfoil whose characteristics allow for optimal performance near the cruise condition. The required maximum cruising speed is Mach 0.85. In order to not suffer from the tremendous drag penalties of supersonic flow over the wing, the airfoil thickness and wing sweep must be chosen such that the critical Mach number is equal to or greater than the maximum cruising condition. There are tradeoffs when selecting these two values. By making the airfoil thinner, the sweep angle can be made smaller which will improve the takeoff and landing performance by increasing the aircraft's $C_{L_{max}}$. This is desirable because of our objective to have a business jet with short

takeoff and landing capabilities. However, when the airfoil is made thinner, the fuel volume of the wing is greatly reduced. In addition, there is less room for wing structure and landing gear storage. Thus, it was decided that a good compromise for obtaining acceptable wing volume while still maintaining aerodynamic capabilities sufficient to satisfy the requirements would be to choose a 10% thick airfoil. From the table on page 150 of Roskam Part II, it was determined that given a critical Mach number of 0.85 and our chosen airfoil thickness, the wing sweep at the quarter chord would need to be 30 degrees [3]. The airfoil was chosen by looking at aircraft with similar missions and cruising speeds. By choosing an airfoil that had been previously selected for use in a business jet or commercial jet application, it would be ensured that the drag characteristics would be appropriate for cruising in the range of Mach 0.7 to 0.85. After narrowing the airfoil selection down to the Gulfstream GIII airfoil and the Boeing 737 airfoil, the decision was made to go with the 737 mid-span airfoil because it had a slightly higher $C_{l_{max}}$ for the airfoil section. This was crucial to our design because of the short takeoff and landing objective. The X-FOIL data for this wing is presented in Table XI while the airfoil section can be seen in Figure 14.



Figure 14. B737c Airfoil Section

Table XI. X-FOIL Data for the B-737c-il Airfoil

α (deg)	C_l	C_d
-4	-0.2928	0.0153
-3	-0.188	0.0114
-2	-0.0818	0.0093
-1	0.0279	0.0082
0	0.1396	0.0082
1	0.2406	0.0064
2	0.3384	0.0058
3	0.4471	0.0052
4	0.5719	0.0068
5	0.7009	0.0079
6	0.8036	0.0093
7	0.8904	0.0105
8	0.9823	0.0122
9	1.0748	0.0146
10	1.1607	0.0179
11	1.2317	0.0204
12	1.288	0.0241
13	1.3103	0.0303
14	1.2961	0.0429
15	1.2452	0.0621

High Lift Devices

The airfoil that was chosen was designed for the Boeing 737. The Boeing 737 has a typical cruising Mach number of about 0.75 which is the same Mach number for our aircraft in the standard cruise configuration. Because this airfoil was designed to have as little drag as possible at high speeds, the $C_{l_{max}}$ is relatively low when compared to low-speed airfoils. While this low $C_{l_{max}}$ of about 1.3 (see Figure 14 and Table XI above) is not ideal in terms of meeting the short takeoff objective, it is necessary to meet the cruise and speed requirements given in the RFP. Any deficiency in $C_{l_{max}}$ of the clean wing will require compensation with high lift devices.

When researching the business jet market, it was determined that there was a void in business jets that could cruise at Mach 0.85, have a maximum range of 2,500 nautical miles at a speed of Mach 0.75 and still access runways around 2,500 feet long. The objective, then, became to design an aircraft with a takeoff distance of 2,500 feet. In the constraint sizing process, it was determined that to achieve the 2,500 ft takeoff distance, the $C_{L_{max}}$ of the wing with the flaps and slats deployed must be 2.1. This value is greater than the value for takeoff and thus represents the constraining case. The first step in achieving this extreme performance was to add flaps to the wings. Looking at similar aircraft on page 195 of Roskam part II, an approximate span wise location of the flaps and ailerons was chosen [3]. Because the flap area needed to be as large as possible, the ailerons were positioned as far out on the wing as practical. From looking at similar aircraft listed in Roskam, the minimum length of the ailerons was determined to be about 15% of the half-span of the wing. Because the wings produce no lift at the tips, the ailerons would have to remain at a distance far enough from the tip to still be effective. The final choice was made to locate the ailerons from 0.80-0.95 of the half-span. The flap span was then chosen to occupy the rest of the space between the fuselage and the ailerons. Doing this yielding flaps that went from 0.15-0.80 of the half-span. The chord length of the flaps and ailerons were chosen to be 0.25 of the chord. This allowed sufficient control surface chord length without sacrificing too much fuel volume that would occur when moving the control surface attachment point (rear spar) too far from the trailing edge. A top-down view showing the planform shape as well as the flap and aileron sizing is shown below in Figure 15.

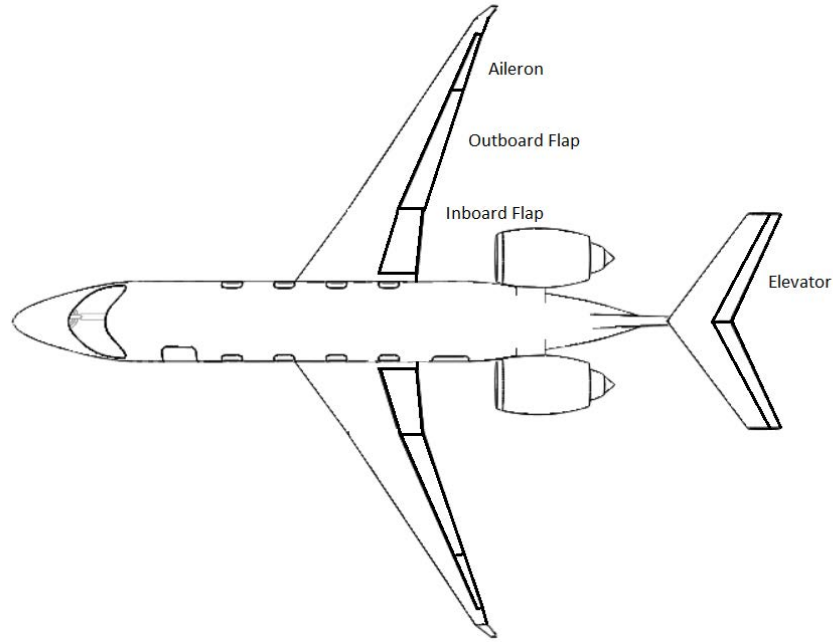


Figure 15. Top-Down View Showing Wing Planform and Control Surfaces

The flap type chosen was the single slotted flap. This type of flap provides excellent incremental lift when compared to a plain flap or split flap while avoiding the complexity of the full Fowler flap. On page 172 of *Roskam Part II*, for the flap-to-chord ratio of 0.25 that was chosen previously, there is almost no difference between the incremental lift between the single slotted and Fowler flaps. Because the Fowler flap would only introduce more weight and complexity into the design with only a small increase in $C_{l_{max}}$, it was decided that the single slotted flap was the correct choice for this application.

In addition to the flaps, leading edge slats were also added to get a higher $C_{L_{max}}$ during takeoff and landing. The slat design increases the chord length by 10% when deployed. The percentage increase in chord length from the slat should increase the $C_{l_{max}}$ of the airfoil section by that same amount [3]. This is summarized in Table XII below.

Table XII. Summary of Increase in $C_{l_{max}}$ of the Wing Section due to Leading Edge Slats

$C_{l_{max}}$ without Slats	$C_{l_{max}}$ with Slats
1.31	1.45

The flap parameters chosen above were optimized such that they combined to yield a $C_{L_{max}}$ that was sufficient to meet the 2,500 ft takeoff objective. The process used to determine if the increment in $C_{L_{max}}$ of the wing due to the flaps is sufficient to meet the required $C_{L_{max}}$ is as follows. First, the $C_{L_{max}}$ of the wing without the flaps deployed must be determined. Comparing this value to the $C_{L_{max}}$ needed for takeoff, the delta needed from the flaps can be determined. The steps to calculate the $C_{L_{max}}$ of the clean wing are as follows. First, the $C_{l_{max}}$ of the wing section must be converted to $C_{L_{max}}$ of the 3D wing. This is done by using Equation (10) below given in *Roskam Part II* [3].

$$C_{L_{max,w}} = 0.95(C_{l_{max,root}} + C_{l_{max,tip}})/2 \quad (10)$$

Next, the lift being produced by the main wing must be slightly greater than the weight of the aircraft to account for the tail down force that is present in this traditional configuration. To take this into account, the $C_{L_{max}}$ of the wing is assumed to have to be 1.05 times the $C_{L_{max}}$ required of the aircraft as a whole. Finally, the wing sweep has to be considered. The $C_{L_{max}}$ of the swept wing will be less than the $C_{L_{max}}$ of the unswept wing. This is accounted for by using Equation (11) below.

$$C_{L_{max,swept}} = C_{L_{max,unswept}} * \cos(\Lambda_c/4) \quad (11)$$

At this point, the $C_{L_{max}}$ required and the $C_{L_{max}}$ of the wing in the clean configuration have been determined. From these two values, the delta needed from the flaps is a simple calculation. These results are summarized below in Table XIII. $C_{L_{max}}$ Increment Needed from the Flaps

Table XIII. $C_{L_{max}}$ Increment Needed from the Flaps

$C_{L_{max,required}}$	$C_{L_{max,clean}}$	$\Delta C_{L_{max}}$
2.10	1.19	0.91

From Table XII above, the required increment in $C_{L_{max}}$ from the flaps is seen to be 0.91. To get this delta which is for the entire wing, the delta for the local section where the flaps are must be even higher. To determine the $C_{l_{max}}$ of the flapped section necessary to get the $\Delta C_{L_{max}}$ of 0.91 for the wing, the equations and graphs outlined on pages 170-175 of *Roskam Part II* were used [3]. Comparing this value to

the $C_{l_{max}}$ that the flapped section is actually capable of determines if indeed the $C_{l_{max}}$ with flaps down of 2.1 is actually achievable. As it turned out, the ΔC_l capable from the flap was not quite large enough to meet the needed requirement. The difference, however, was small and only increased the takeoff distance to only 50 feet longer than the objective. These differences are shown in below.

Table XIV. ΔC_l Needed from the Flap Compared to the. ΔC_l Capable from the Flap

ΔC_l Needed from Flap	ΔC_l Capable from Flap	Takeoff Distance
1.79	1.76	2,550 ft

The wing section as designed with both flaps and slats fully deployed is shown in Figure 16 below.

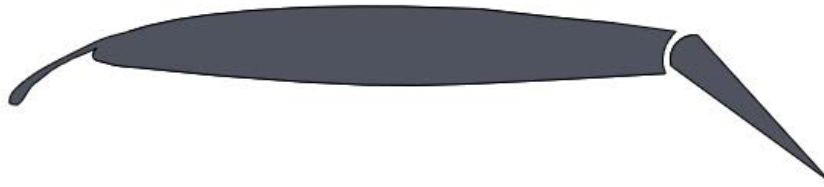


Figure 16. Airfoil Section Showing Full deployments of Flaps and Leading Edge Slats

This high-lift capability coupled with the high-thrust capabilities from the engines yields a takeoff distance of about 2,550 feet. This comes extremely close to meeting the 2,500 feet objective and puts this aircraft in a performance category unmatched by existing business jets.

Empennage

The design procedure of the empennage is directly borrowed from Dr. Jan Roskam’s *Airplane Design Part II*, which is a Class I method of tail sizing [3]. Once the conceptual empennage and fuselage configuration was determined as T-tail and its location with respect to an approximate center of gravity, the so-called \bar{V} -method was utilized in designing the horizontal and vertical tails. The following equations are the volume coefficients for the horizontal and vertical tails, respectively.

$$\bar{V}_h = \frac{x_h S_h}{S \bar{c}} \quad (12)$$

$$\bar{V}_v = \frac{x_v S_v}{S b} \quad (13)$$

where the h and V subscripts denote the horizontal and vertical tails, respectively, x is the moment arm from the tail surface quarter chord, $S_{h,v}$ is the reference area for the respective surface, S is the main wing reference area, \bar{c} is the main wing mean geometric chord, and b is the span of the main wing. Once the main wing area, span, and mean geometric chord were determined, the other necessary tail parameters such as the moments arms and volume coefficients can be determined statistically from Class I methods, i.e. by applying averages of aircraft of similar MTOW, overall configuration, performance, and mission. These values then can be plugged back into the volume coefficient equations to arrive at a reasonable estimate for the horizontal and vertical tail areas. Table XV below represents the Class I data obtained from Roskam Part II.

Table XV. Class I statistical data for the empennage.

Aircraft	S (ft²)	\bar{c} (ft)	S_h (ft²)	S_v (ft²)	\bar{V}_h	\bar{V}_v	x_h (ft)	x_v (ft)
Learjet 24	232	7.03	54	38.4	0.67	0.077	20.2	16.6
SN-601	237	5.6	58.9	45.4	0.74	0.071	16.7	15.7
MU Diam.I	241	6.23	57.2	55.9	0.85	0.093	22.4	17.4
<i>Averages</i>	<i>236.67</i>	<i>6.29</i>	<i>56.70</i>	<i>46.57</i>	<i>0.75</i>	<i>0.08</i>	<i>19.77</i>	<i>16.57</i>

The average values shown in the last row were used for the horizontal tail with some corrections as the wing geometry averaged from the three aircraft do not match the Coronis aircraft. It is important to note here that the determination of the horizontal tail characteristics is much less cumbersome compared to the vertical tail, hence the horizontal tail parameters were considerably more influenced from Class I statistical data. The vertical tail on the other hand requires an analysis of the one-engine inoperative condition to determine its size which will be explained later in this section. The horizontal tail parameters were chosen to be quite close to the statistical data, which is summarized in Table XVI.

Table XVI. Horizontal Tail Parameters

\bar{V}_h	x_h (ft)	S_h (ft ²)	b_h (ft)
0.79	22.6	55.2	15.8

Although the initial sizing is presented up until this point for the horizontal tail, there still are parameters that are missing which are essential to its design such as the taper ratio, sweep, dihedral angle, incidence angle, and aspect ratio. A similar approach was taken to determine these quantities as the initial sizing of the horizontal stabilizer. The following values were selected from Roskam Part II describing the common values for the planform design parameters for the tail; the values concerning the business jet category are reproduced in Table XVII below [3],

Table XVII. Statistical Empennage Planform Parameters

	Γ (deg)	i (deg)	A	$\Lambda_{c/4}$ (deg)	λ
Horizontal Tail	-4 - +9	-3.5 fixed	3.2 - 6.3	0 - 35	0.32 - 0.57
Vertical Tail	90	0	0.8 – 1.6	28 - 55	0.30 – 0.74

where Γ is the dihedral angle, i is the incidence angle, A is the aspect ratio, $\Lambda_{c/4}$ is the sweep at quarter chord, and Λ is the taper ratio. Using these values given above as a guide, reasonable decisions have been made concerning the dihedral angle, aspect ratio, and taper ratio. Interestingly, the incidence angle proved to be quite different from the subsequent trim analysis. As a matter of fact it was determined not to be negative as suggested by the Class I analysis, but ranging from +0 to about +2 degrees for the 6- and 8-seater variants, respectively. This was because the center of gravity of the both Coronis variants are between the center of pressure of the main wing and the tail. Hence, positive lift was required from the horizontal stabilizer to counteract the pitch-up moment produced by the main wing. This will be further explored in the “Trim Analysis” heading in the latter sections of this paper.

Choosing the symmetrical NACA 0008 airfoil for the horizontal tail which was driven by statistical data of similar airplanes, the sweep was determined according to the limiting factor of the critical Mach number (M_{CR}). According to Roskam Part II, a thickness-to-chord ratio of 0.08 and sweep angle of 34°

results in an M_{CR} of 0.88 at a $C_L = 0.4$ [3]. The main wing has an M_{CR} of 0.86 which is less than that of the horizontal tail as required by stability concerns. If the tail achieves the critical Mach number before the main wing, losing control effectiveness in the elevator due to the increased drag and decreased lift may result in undesirable characteristics during max cruise speed of Mach 0.85.

A similar analysis was carried out for the vertical tail to determine the planform parameters. Due to the T-tail configuration which led to increased loads because of the location of the horizontal tail attachment, it was found to be reasonable to select a thicker symmetrical airfoil: NACA 0012. M_{CR} was found to be 0.87 for a sweep of 43° which satisfies the requirement of having the tail M_{CR} higher than that of the main wing. The rest of the parameters were chosen as the average values from the statistical planform value from Roskam Part II and they are, along with the horizontal stabilizer, summarized in Table XVIII.

Table XVIII. Empennage Planform Parameters

	Γ (deg)	A	$\Lambda_{c/4}$ (deg)	λ
Horizontal Tail	-1	4.5	34	0.566
Vertical Tail	90	1.2	43	0.4618

The incidence angle of the horizontal stabilizer was not included as it was determined through AVL within trim analysis. The dihedral was chosen to be -1° for aesthetic purposes inspired by the Dassault Falcon 50/900, which also will provide somewhat more directional stability due to increased damping in the yaw direction. This was purely a design engineer “gut feeling” and turned out to be sound judgement as the Dutch roll mode of the Coronis 6 & 8 was not found to adhere to the Level 1 Flying Qualities without a Stability Augmentation System (SAS). The aspect ratios used for both surfaces are simply the averages of statistical data. Having a lower aspect ratio on the horizontal stabilizer is necessary to counteract the positive incidence angles found for trim conditions to assure that the low aspect ratio allows the horizontal surface to stall later than the main wing.

The taper ratios were calculated through iterations of determining the necessary geometry of the horizontal and vertical stabilizer with the given reference area, sweep, and aspect ratio, resulting in a unique

solution for λ . The calculated values for this parameter decently fit into the Class I statistical data provided by Roskam Part II on business jets, being on the higher end of taper ratios.

The vertical tail sizing is directly driven by the one-engine inoperative condition since that is the most critical condition that the surface needs to be sized for. The vertical tail and the rudder surface should have the necessary control authority to counterbalance the yawing moment created by the critical engine, for instance during an engine failure during takeoff at V_{mc} . The following relation was used to determine the critical engine-out yawing moment.

$$N_{t_{crit}} = T_{TO_e} y_t \quad (14)$$

where $N_{t_{crit}}$ is the critical engine-out yawing moment, T_{TO_e} is the takeoff thrust of one engine, and y_t is the lateral thrust moment arm of the most critical engine. Secondly, the drag-induced yawing moment due to the inoperative engine was calculated using the following equation.

$$N_D = 0.15 N_{t_{crit}} \quad (15)$$

where N_D is the drag-induced yawing moment. Lastly, the rudder deflection required to hold the engine-out condition is calculated from the following formula.

$$\delta_r = \frac{N_D + N_{t_{crit}}}{\bar{q}_{mc} S b C_{n_{\delta_r}}} \quad (16)$$

where δ_r is the rudder deflection, \bar{q}_{mc} is the dynamic pressure at V_{mc} , and $C_{n_{\delta_r}}$ is the control derivative of the yawing force n with respect to the rudder deflection. This rudder deflection may not be greater than 25° and in fact, it was calculated to be less than 12° . In other words, this result means that merely a 12° deflection of the rudder will be sufficient in counteracting the yawing moment during a one engine inoperative state.

Plugging in the values obtained from the engine thrust, location of the engines with respect to the y-axis of the airplane, and an estimated preliminary control derivative from Nelson of -0.063, the following Table XIX summarizes the geometry of the vertical tail.

Table XIX. Vertical Tail Parameters

\bar{V}_v	x_v (ft)	S_v (ft ²)	b_v (ft)
0.080	16.57	60.99	8.56

As expected, these values match the statistical averages of the three aircraft made earlier. The final design decisions of the tail which is the same for both Coronis 6 & 8, can be seen in Figure 17 below.

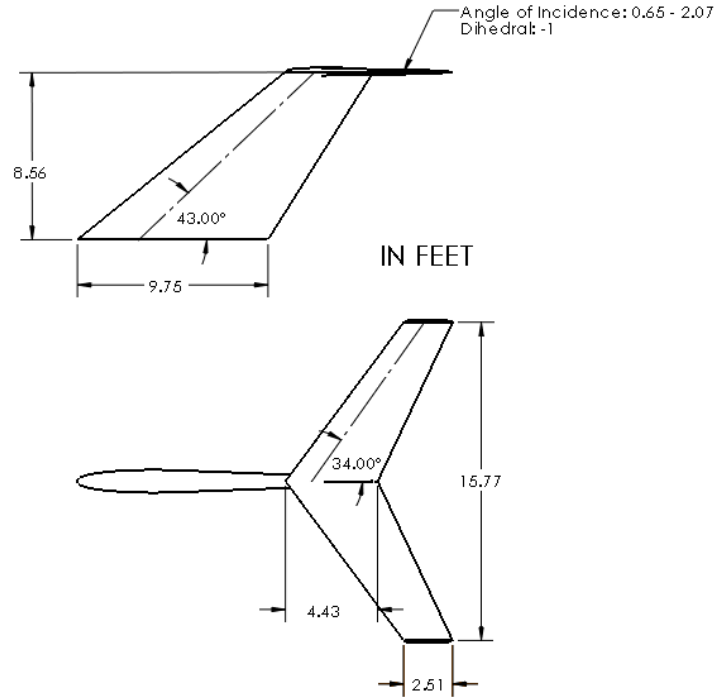


Figure 17. Geometry of the Empennage

The empennage weight was estimated using Roskam Part V using the Torenbeek Method which applies to transport airplanes and business jets with design dive speeds above 250 knots [4]. The Coronis 8 has a design dive speed of 341 EAS knots which fits the assumptions of the method. The following relation was used in determining the weight of the horizontal tail.

$$W_{h,v} = K_{h,v} S_{h,v} \left[\frac{3.81 S_{h,v}^{0.2} V_D}{1,000 \cos\left(\frac{1}{2}_{h,v}\right)^{0.5}} - 0.287 \right] \quad (17)$$

where the h and V subscripts denote the horizontal and vertical tails, respectively, $W_{h,v}$ is the weight, K_h is 1.0 for fixed-incidence stabilizers, V_D is the design dive-speed, $\frac{1}{2}_{h,v}$ is the semi-chord sweep angle, and

$$K_V = 1 + 0.15 \frac{S_h z_h}{S_V b_V} \quad (18)$$

which is for fin mounted horizontal tails where z_h is the distance from the vertical tail root to where the horizontal tail is mounted on the vertical tail. With these values easily obtained from the geometry and performance of the Coronis aircraft, the following weights are obtained for the empennage sections shown in Table XX.

Table XX. Tail Weights

	Weight (lbs)
Horizontal Tail	160.11
Vertical Tail	219.77

These numbers are actually projected to be conservative since a technology factor has not been applied. The Coronis will be using composite materials in the lifting surfaces which will make 20% of the total empty weight lighter than it currently is projected to be.

Propulsion

To achieve the desired design point of short take-off, high-thrust engines are required. Constraint analysis details a required thrust of 8,500 lbf, or 4250 lbf per engine. Further, the requirement of Mach 0.85 cruise limited propulsion options to turbofan and turbojet engines. An analysis of various jet engines on the market was performed, and of the engines surveyed, only five met the thrust requirement. Of these, the Honeywell TFE731-40AR was selected due to its reduced TSFC, smaller size, and lower weight compared to the other engines. Its characteristics are presented in Table XXI.

Short landings are also desired, to fully operate on short runways; to meet this requirement, thrust reversers are required. Safran Nacelles provides Planar Exit Rear Target (PERT) thrust reversers [5] which are implemented with the Honeywell TFE731-40AR.

Table XXI. Specifications for the Honeywell TFE731-40AR jet engine.

Parameter	Value	Reference
Thrust, Continuous (lb)	4250	[6]
Thrust, Takeoff (lb)	4420	[7]
Weight (lb)	885	[6]
TSFC	0.46	[8]
Length (in)	60.91	[6]
Diameter (in)	39.36	[6]

Auxiliary Power Unit (APU)

Power for electrical systems and bleed air for pressurization, anti-ice protection, air conditioning, and engine starting are provided by an APU. APUs used in similar jet aircraft were surveyed, and the Honeywell RE100 was selected due to its small size, low weight, performance, and current market availability. Its specifications are presented in

Table XXII. This APU is ideal, as it is the smallest surveyed which can provide bleed air necessary maintain a pressurized cabin to our flight ceiling of 45,000 ft.

Table XXII. Specifications for the Honeywell RE100 APU.

Parameter	Value	Reference
Weight (lb)	83	[9]
Power (shp, kW)	23, 17	[9]
Bleed air (lb/min at 36 psig)	35	[10]
Dimensions (L, W, H) (in)	27.2, 17.3, 16.1	[10]
Cabin Altitude at FL450 (ft)	6,800	[11]

8. Performance

Aerodynamics

The aerodynamic analysis of the aircraft was completed using Star CCM+. To run the Computational Fluid Dynamics (CFD) analysis, a water tight CFD mesh stl file was exported from the VSP model. The stl model was then imported to Star CCM+ as a 3D part. A box shaped flow field covering the

right half of the aircraft was created with dimensions that were 10 times the length of the fuselage to ensure the flow field was big enough to capture all the flow around the aircraft and capture the freestream conditions at the edge of the box. Only half of the aircraft was analyzed, because the aircraft was symmetric across the x-z plane. By only analyzing half of the aircraft, the run time was decreased by half. The aircraft surface was subtracted from the box to get the flow area of interest. The subtracted geometry was assigned to a region for analysis.

Surface and volume controls were used to create variable sized mesh to minimize calculation time. Surface mesh control was used on the boundaries of the flow field to obtain finer mesh near the aircraft and coarser mesh farther away in the freestream. Another surface mesh control was used on the surface of the aircraft to create finer mesh on the aircraft surface. To obtain more accurate results at the leading edge of the wings, two cylinder parts were created and placed at the leading edge of the wing. Volume control was used for these cylinders to create finer mesh at the leading edge. To capture the boundary effects without significantly increase the run time, eight prism layers were created. A volume mesh was generated on the subtracted geometry with these surface and volume controls using trimmed cell mesher.

In Star CCM+, the flow conditions were set up as a physics continuum. The physics continuum had the cruise altitude pressure as the reference pressure and the initial conditions with cruise altitude temperature and velocity. In the regions section, the boundaries were set up as freestream, symmetry, and wall. The freestream physics values were set up with cruise Mach, static temperature, and flow direction. The solvers used were 3D solvers with coupled implicit and K-Omega Turbulence model with stopping criteria of 2000 iterations. The C_L and C_D reports were set up using the cruise velocity, half of wing reference area, and air density. The L/D report was set up by dividing the C_L report by the C_D report.

Three simulations were run to obtain the drag polar of the aircraft at three different angles of attack (1, 4, and 8 degrees). The simulations were stopped after C_L , C_D , and L/D converged. Figure 18 shows the drag polar of the full aircraft without the pylon and engine based on the CFD analysis using Star CCM+ for cruise condition specified in Table XXIII. The cruise condition required a C_L of 0.4, so the flight angle of attack was at 1 degree. The ratio lift over drag (L/D) as a function of angle of attack is shown on Figure 18.

Figure 19 shows the Mach number distribution over the aircraft at cruise condition. As shown on the figure, at the tip of the wing, several shocks could be identified, because the volume mesh had some sharp edges at those locations. Therefore, on the actual wing, the wing would have remained subsonic for the cruise condition.

Table XXIII. Cruise condition

Mach	0.75
Altitude (ft)	41,000

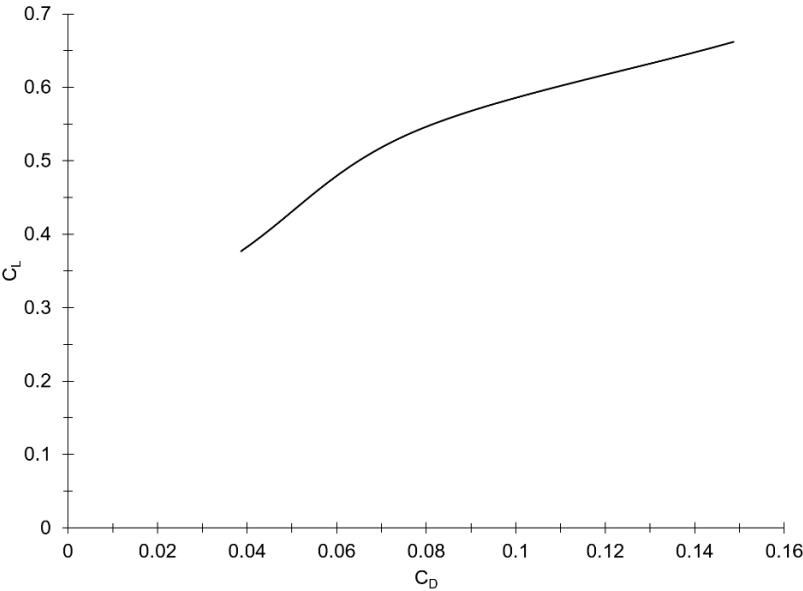


Figure 18: Drag Polar of 8S without Pylon or Engine from CFD

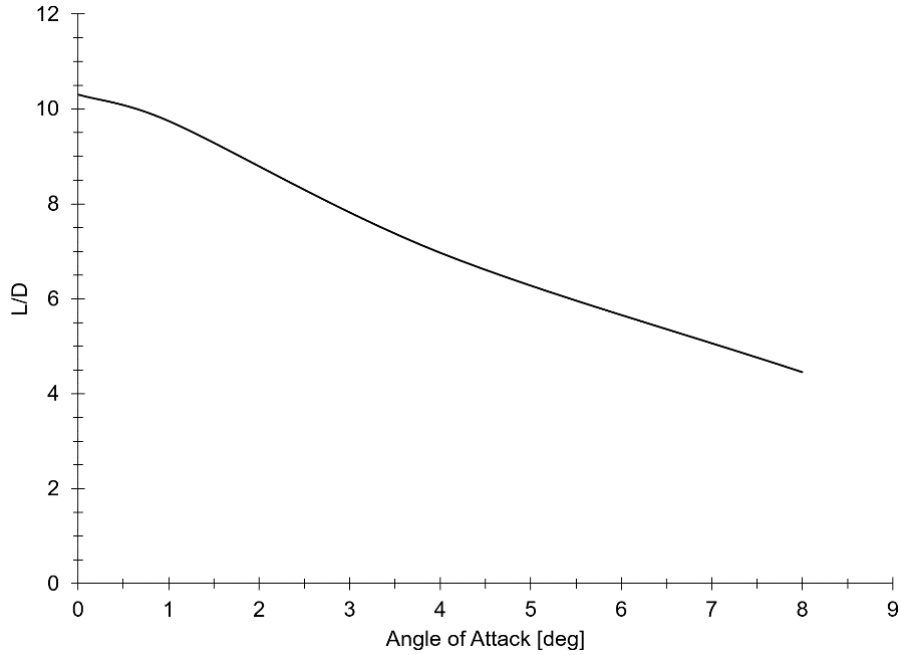


Figure 19. Variation of L/D with Angle of Attack of 8S from CFD

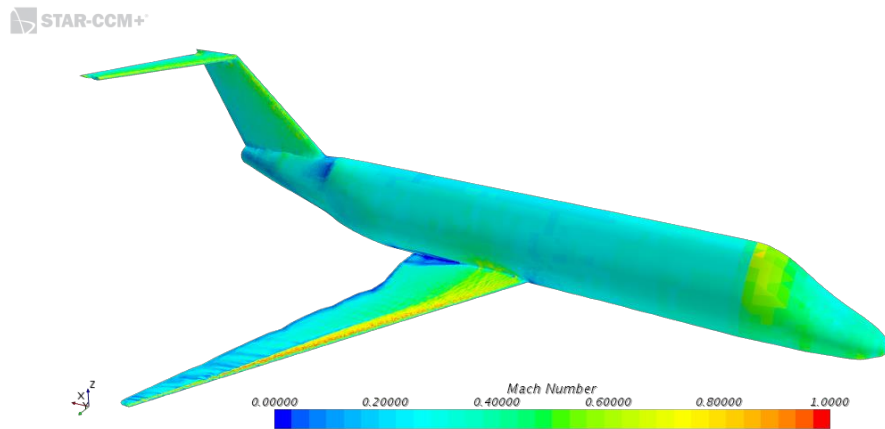


Figure 20. Mach Number Flow Visualization around 8S

Takeoff

Takeoff and landing lengths were calculated using the energy based approach described in Aircraft Engine Design [12]. The takeoff length accounts for ground roll, rotation distance, flight in ground effect, and steady airborne climb. As required by the RFP, the takeoff distance for both the six and eight seat variants to clear a 35 ft obstacle must not be greater than 4000 ft at standard atmospheric conditions. The

takeoff capability of the eight-seat variant, the 8S, is shown below in Figure 21. Note a total field length of 2,550 ft at sea level at standard atmospheric conditions which clearly exceeds the RFP requirements.

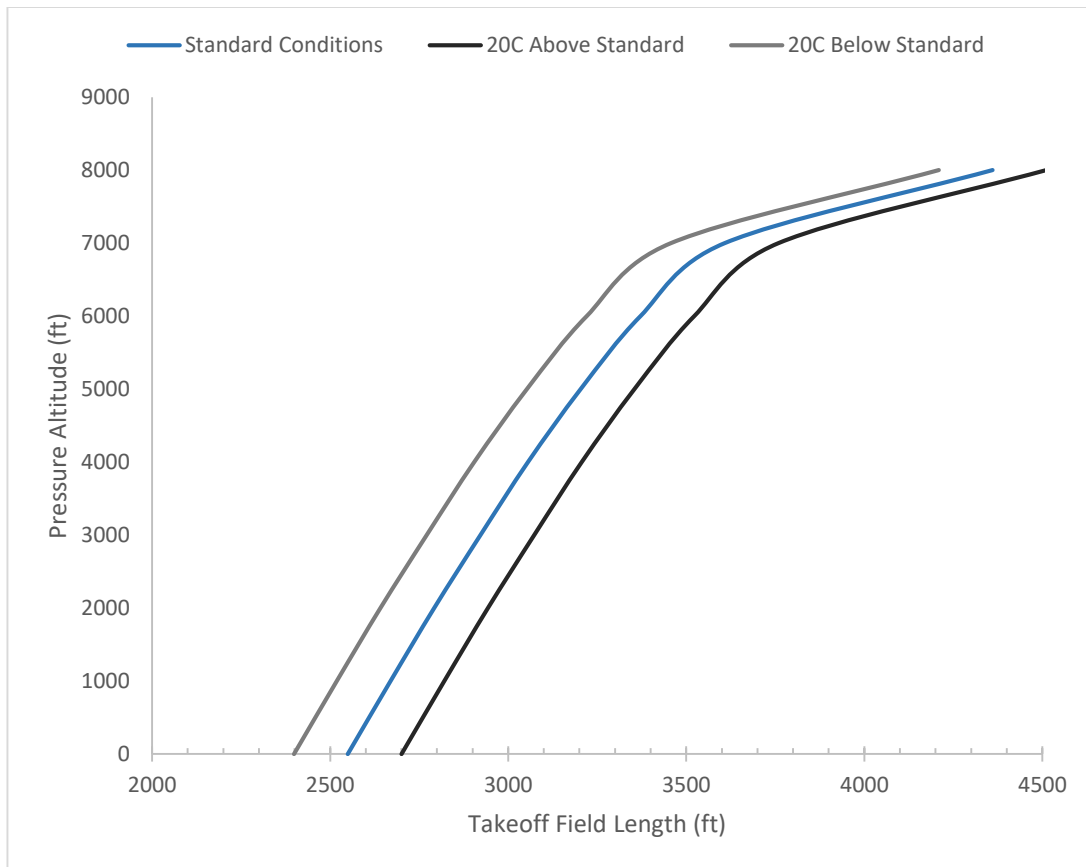


Figure 21. Eight Seater Takeoff Performance

Such excellent performance in takeoff distance was intentionally sought after in initial constraint sizing to meet the intended mission of the aircraft in reaching small and out-of-the way airport and grass strips. Such short distance provides great versatility in providing flexibility to the customer and operator.

Range

The RFP required both aircraft variants to be able to carry the specified payload over the previously discussed 2500 nautical mile IFR range profile. Both aircraft met these requirements with the 6s exceeding them slightly due to reduced cabin frame and payload weights. Payload – Range charts for both aircraft are given below in Figure 22 and Figure 23, respectively.

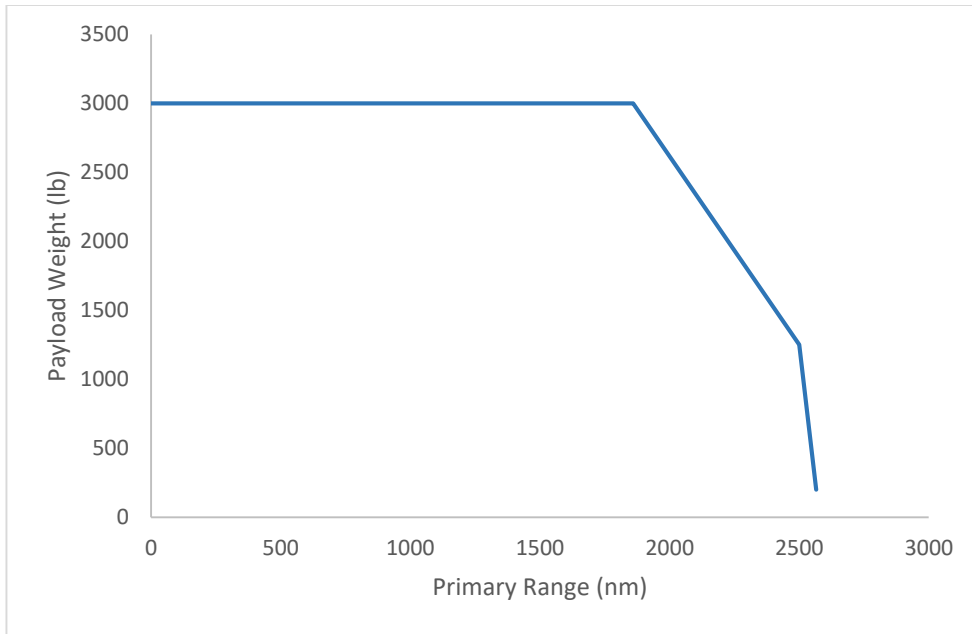


Figure 22. 8S Payload Range Profile

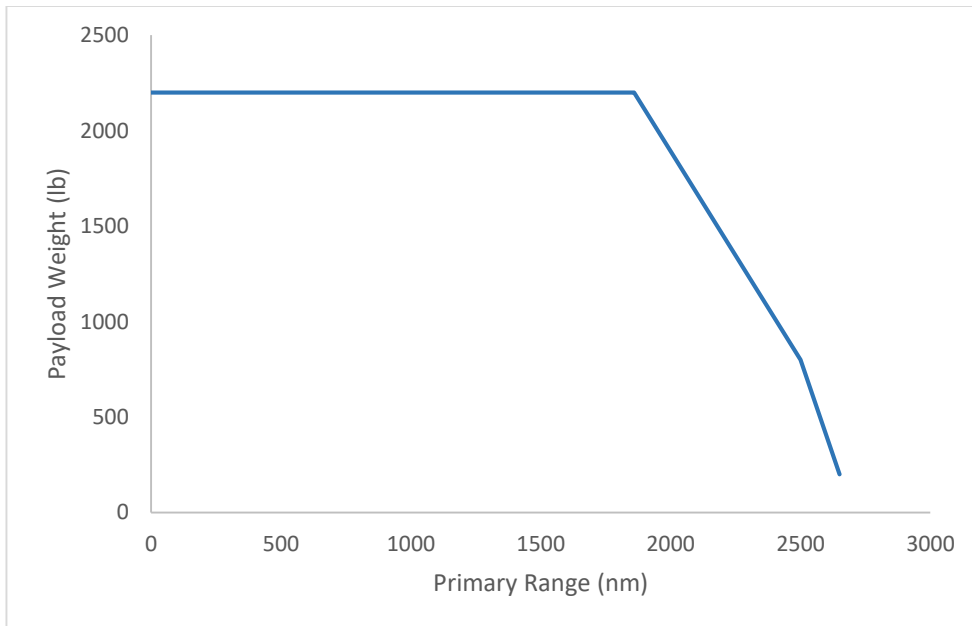


Figure 23: 6S Payload Range Profile

V-N Diagram

The V-n diagram for the required Part 23 performance envelope of the Coronis family of aircraft were developed to show the inertial loads the aircraft must be able to endure and is shown below in Figure 24. Inertial loads of +2.95/-1 are shown by the limiting horizontal lines. Gust speeds and dive limitations imposed by Part 23 were also met. Note that the cruise speed of the aircraft was determined to be 275 KEAS as determined from the established 0.75 Mach cruise speed used at 35,000 ft for weight sizing.

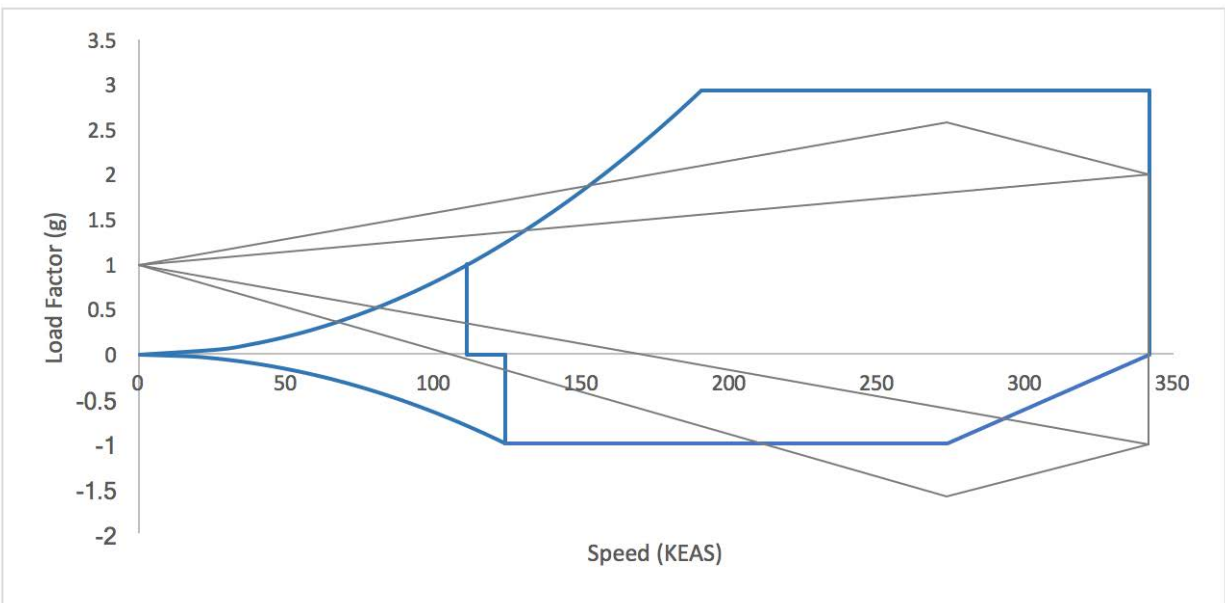


Figure 24: 8S V-N Diagram

9. Structure and Manufacturing

Material

The material selection of several main components of the aircraft was considered. These were the fuselage, wings, empennage, and landing gear. The use of composite materials was considered for the aircraft for the weight-savings and the increase in performance. However, with the potential of many composite components, the overall manufacturing and maintenance costs would increase which would

subsequently increase the cost to the consumer. This would decrease the affordability of the aircraft which may affect the future sales in this competitive area of commercial aviation.

As a compromise, an all-composite fuselage was used. This is the largest (spatially) of the components and would most likely need fewer component changes and maintenance alterations in the future. The decrease in weight from using a composite fuselage can aid in an increase in the overall performance of the jet. A carbon fiber reinforced polymer composite with epoxy was chosen as the material for this component of the aircraft. There are many benefits to choosing carbon fiber such as its high rupture resistance, good fatigue strength, and small specific mass. To avoid potentially negative consequences such as damages from lightning, a protective aluminum film is used.

The material of the wings was chosen to be the conventional high grade aluminum alloy commonly found in commercial airlines. The specific aluminum alloy chosen was aluminum 7075. Aluminum was chosen for a variety of reasons that include its reliability, light weight, and affordability. This material is more likely to have an even distribution whereas their composite counterparts may have defects in the castings. It also has anticorrosion characteristics that can potentially lower the frequency of maintenance. These benefits, along with its reliability are important to ensure the high loads the wings must take during its expected short take-off and landings.

The empennage material was chosen to be a boron epoxy composite for the vertical and horizontal stabilizer boxes. This material is good as it has high rupture resistance, high rigidity, and good fatigue resistance. This, in conjunction with the composite structure of the fuselage, will allow for greater weight savings for the aircraft.

The landing gear must take high impact loads since it must support to entire weight of the aircraft, which results in the need for a material that is sturdy with high toughness and strength. The most common materials for landing gear types are steel and titanium. A titanium alloy, titanium 6-4, was chosen in lieu of steel alloys such as 300M. The landing gears must be able to be used in soft ground runways, which places stress on steel.

Wing Structure

The wing structure for the aircraft consists of two spars running the length of the wing as well as ribs at 26.7 inch intervals. Both spars consist of typical aluminum C-section with the main spar being located $0.20c$ from the leading edge while the secondary spar is located $0.75c$ from the leading edge. The location of the main spar is far enough back from the leading edge to allow sufficient thickness to handle the required loads while not being too far back in order to balance the need to have enough volume between the two spars in order to store the fuel. For the secondary spar, the location was determined by the previously determined control surface locations. Because the ailerons and flaps have a length of $0.25c$, the secondary spar is located this same distance from the trailing edge such that these surfaces can attach directly to the spar.

The ribs are constructed of aluminum sheet metal 0.10 inches thick and are placed every 26.7 inches along the span of the wing. Circular cutouts are used to reduce the weight of each rib while also allowing for fuel cross-flow through the wing as well as for deicing tubes that will run along the wing's leading edge. The rib structure is shown in Figure 25 below.



Figure 25. Wing Rib

After implementing the design as defined above, the wing structure looks as shown in Figure 26 below. Here, cutouts in the wing structure behind the secondary spar are representative of where the flaps and ailerons would be mounted.

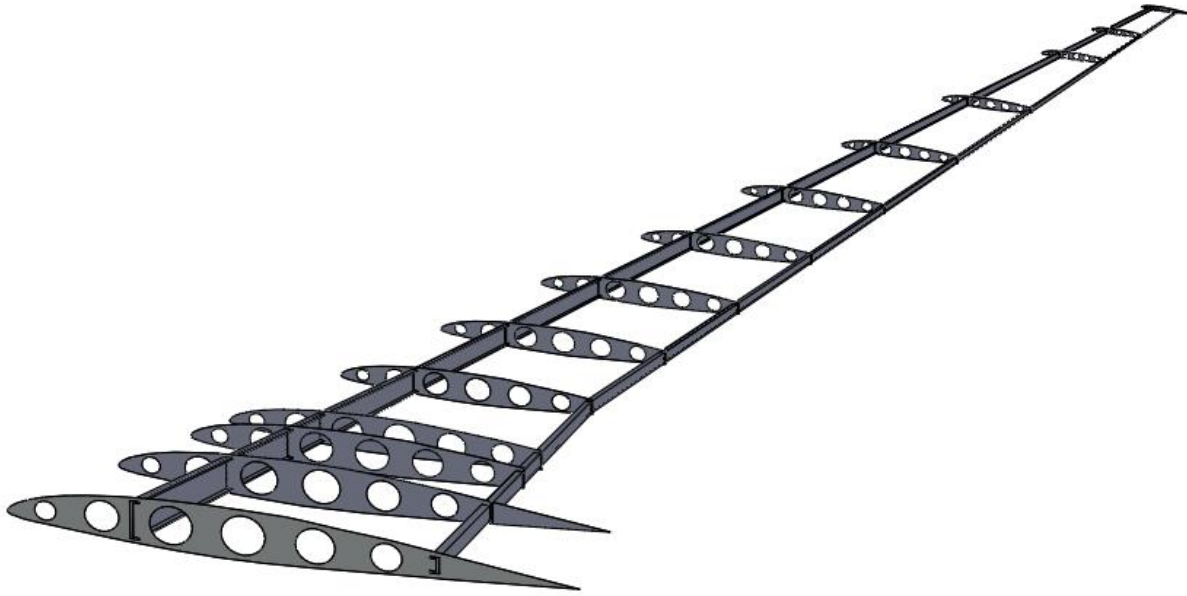


Figure 26. Wing Structure Showing Rib and Spar Placement and Control Surface Cutouts

Static Analysis

Once the design of the wing structure of the aircraft was finalized, verification that the structure strength would be able to sustain the loads during normal flight was conducted using finite element analysis (FEA) . The analysis was performed under the maximum cruise speed expected, Mach 0.85, and the maximum weight of the 8-seater variant, 18,400 lbs. The shell properties for the model analyzed was a constant thickness of the chosen material, aluminum. From this analysis, several attributes of the deformed wing can be observed. In Figure 27., the wing displacement can be seen for the aircraft in cruise conditions. A maximum displacement of 14.6 inches can be seen on the wingtips of the wing and a minimum displacement of 0 inches at the base of the wing. The stress distribution of the wing is shown in Figure 28, with the maximum stress being 52,200 psi or 360 MPa at the tip of wing and the minimum stress being 189 psi or 1.303 MPa.

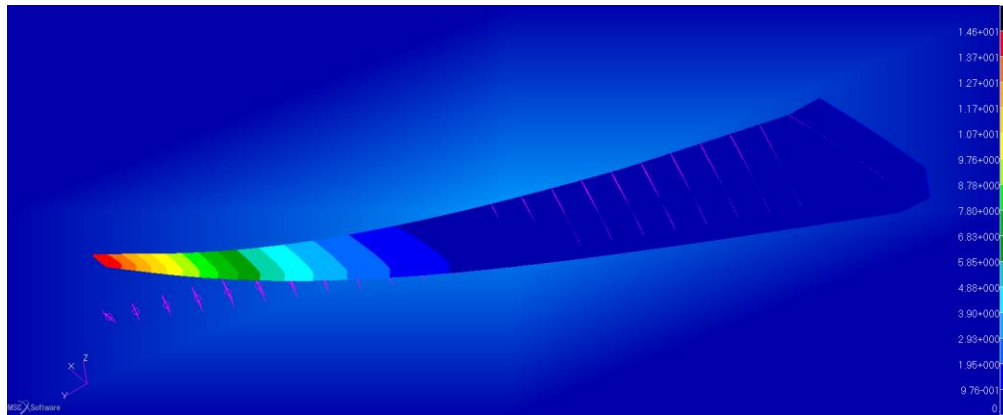


Figure 27. Wing Displacement at Maximum Load

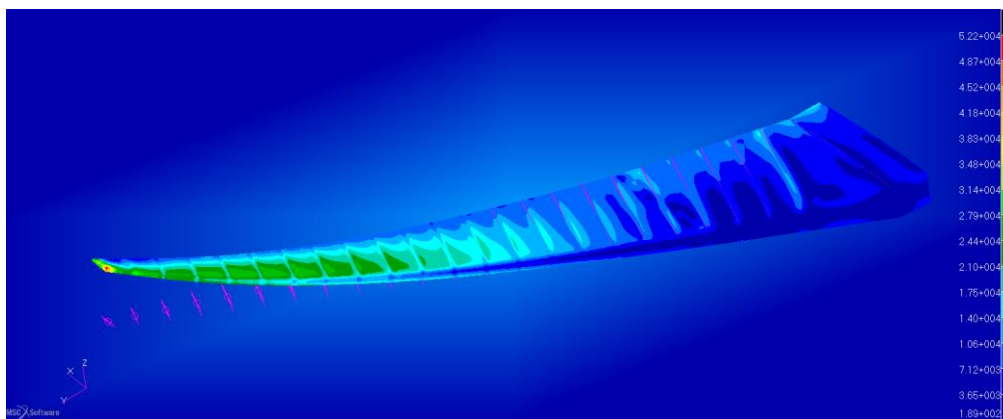


Figure 28. Stress Distribution of Wing at Maximum Load

The highly loaded wingtips in the finite element analysis resulted in a large amount of stress and displacement at the wingtips. These results of the wing may stem from design factors of the wing related to the twist of the wing and the small taper ratio. The material chosen for the wing was Aluminum 7075 which, untreated, has a maximum yield strength of 140 MPa. This is lower than the maximum stress experienced on the wing. However, it is important to note that the FEA conducted on the wing is only a type of preliminary analysis that does not entirely represent the exact maximum loads that are induced onto the wing and there are options of treated aluminum 7075 which has maximum yield strengths much greater than the maximum stress seen in the simulation.

From the analysis on the wing, an estimated spar and rib placement can be generated. The spar and rib placement suggestions are shown in Figure 29. These placements are similar to and verify the initial placements designed based on the Roskam texts.

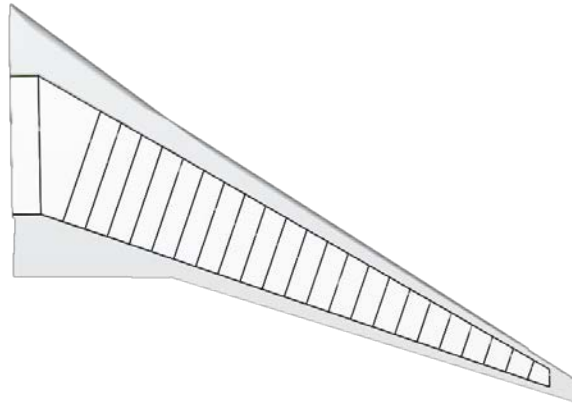


Figure 29. Spar and Rib Placement for FEA Analysis

The analysis conducted on the wing in FEA can be also completed for other components of the aircraft such as the empennage and fuselage. In order to understand the total loads sustained on the aircraft and to verify the material choices stated previously, further analysis must be completed.

Landing Gear

Designing appropriate landing gear was important to ensure the plane could accommodate unimproved runway surfaces. Despite the advantage of conventional landing gear being well suited for handling rough terrain, a tricycle landing gear arrangement was chosen for safety and aesthetic reasons. Taxiing visibility and control is significantly better on a tricycle system and since taildraggers are typically found on older aircraft and small general aviation aircraft, we figured our customers would not view a tail dragging jet as progressive but rather a step backward.

The main landing gear features a two-wheel suspension system with an oleo shock absorber and trailing link as shown in Figure 30. Trailing link landing gear is excellent at handling rough terrain which is needed for landing on unimproved surfaces. Another benefit is that the wheel contacts the ground aft of the main strut of the landing gear, which improves the longitudinal tip over criteria for the aircraft. This tip

over criteria ensures that at maximum deceleration on the ground the aircraft does not tip over, and moving the main gear contact point aft improves this stability. The nose landing gear features a single wheel with oleo strut. The nose gear is controlled by a nose wheel steering wheel on the pilot side of the aircraft.



Figure 30. Main Landing Gear with Oleo Shock Absorber and Trailing Link

Retractable gear seemed the obvious choice for an aircraft capable of traveling at Mach 0.85. The main gear struts are mounted to ribs on the wing and retracted under hydraulic power into the belly of the fuselage. Figure 31 shows how the main gear fits into the wing-body fairing.

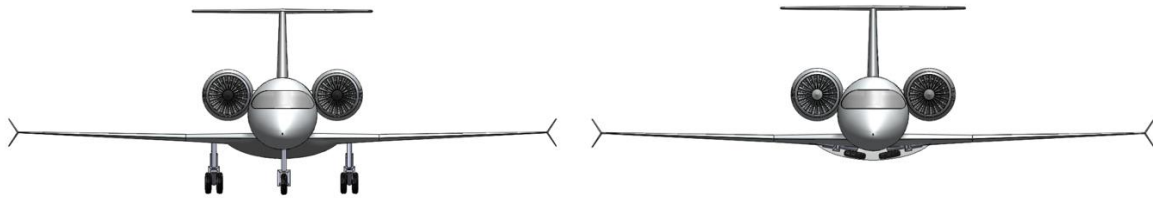


Figure 31. Front View of Aircraft with Landing Gear Extended and Retracted

To take up less space in the nose and allow more room for the weather radar, the nose gear retracts forward and rotates 90°. This is better shown in the isometric view of the aircraft in Figure 32.

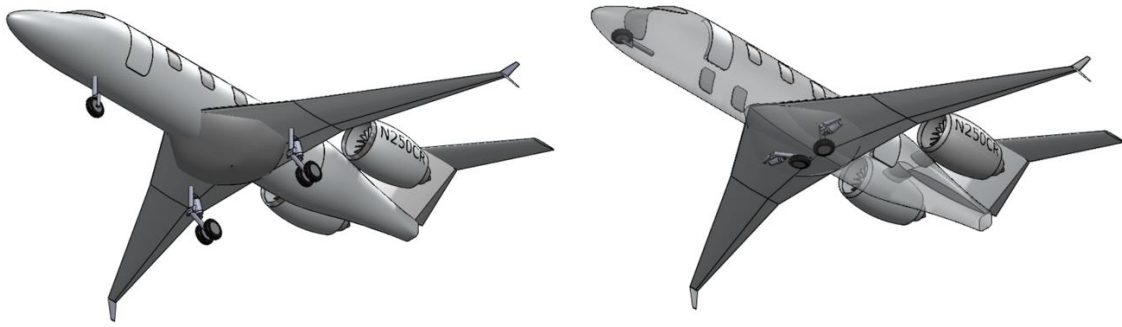


Figure 32. Isometric View of Aircraft with Landing Gear Extended and Retracted

10. Weight and Balance

The weight and balance analysis of the aircraft began with estimating the weight fractions of each component and placing them at their approximate location on the aircraft. Assuming each component as a point mass and inputting the neutral point from the vortex lattice model, the center of gravity and longitudinal static margin could be visualized.

8S Weight and Balance

The weight fractions of the 8S were averaged for many small light business jets. These weight fractions were multiplied by the weight of the aircraft and adjusted by a common multiplier until the final weight of the aircraft was equal to the estimates from the weight regression estimate. These weights are given in Table XXIV.

Table XXIV. Major Subassembly Weights for 8S Aircraft

	Fraction	Initial Estimate (lb)	Adjustment (lb)	Subassembly Weight (lb)
Wing/GW	0.098	1,803	180	1,983
Empennage/GW	0.024	442	44	486
Fuselage/GW	0.105	1,932	193	2,125
Landing Gear/GW	0.039	718	72	789
Propulsion/GW	0.082	1,509	151	1,659
Fixed Equipment/GW	0.166	3,054	305	3,359
Empty		9,458		10,402
Crew				200
Operating Empty				10,602
Payload				1,050
Fuel				6,748
Gross Weight				18,400

These subassemblies were broken into smaller components and assumed to be point masses around the aircraft. These components give the mass properties of the aircraft as shown in Table XXV which is shown visually in Figure 33.

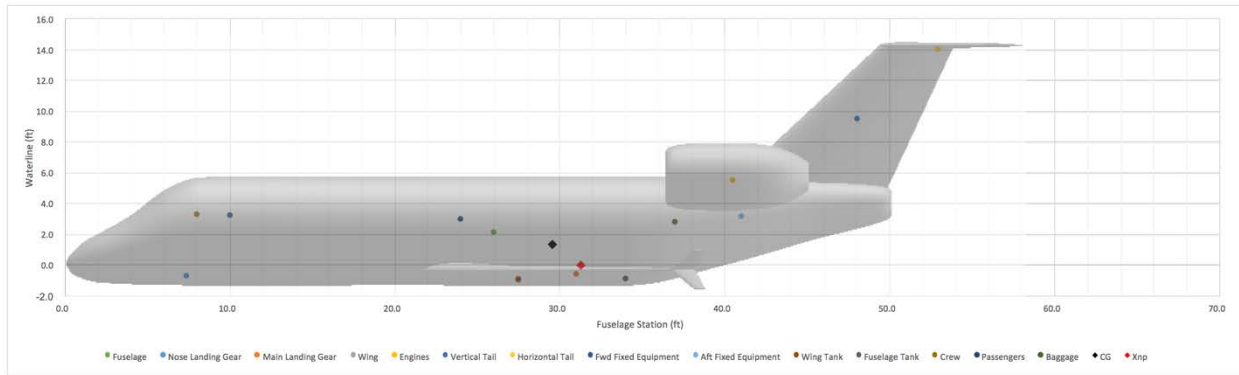


Figure 33. Point Mass Distribution of 8S at MTOW

Table XXV. Mass Properties of 8S Aircraft

	Weight (lb)	X arm (ft)	Y arm (ft)	Z arm (ft)	X Moment (ft.lb)	Y Moment (ft.lb)	Z Moment (ft.lb)	I _x (sl-ft ²)	I _y (sl-ft ²)	I _z (sl-ft ²)
Fuselage	2,125	26.0	2.0	2.1	55,248	4,240	4,415	674	854	1,082
Nose Landing Gear	263	7.4	0.4	-0.7	1,944	113	-186	229	4,037	4,004
Main Landing Gear	526	31.0	2.2	-0.6	16,311	1,159	-318	517	98	115
Wing	1,983	27.5	11.3	-0.9	54,539	22,492	-1,787	9,768	563	8,174
Engines	1,659	40.5	3.6	5.5	67,208	5,996	9,127	717	7,100	6,883
Vertical Tail	307	48.1	0.0	9.5	14,743	2	2,914	231	3,907	3,274
Horizontal Tail	179	52.9	3.0	14.0	9,473	534	2,505	543	3,937	3,097
Fwd Fixed Equipment	1,512	10.0	1.6	3.2	15,117	2,393	4,881	203	18,060	18,011
Aft Fixed Equipment	1,848	41.0	0.9	3.2	75,754	1,663	5,833	162	7,747	7,605
Wing Tank	4,093	27.5	9.6	-0.9	112,567	39,407	-3,873	15,655	1,188	12,302
Fuselage Tank	2,655	34.0	1.6	-0.9	90,267	4,247	-2,454	2,703	2,078	1,864
Crew	200	8.0	1.3	3.3	1,600	252	651	21	2,900	2,887
Passengers	800	24.0	1.7	2.9	19,200	1,336	2,356	135	821	827
Baggage	250	37.0	1.3	2.8	9,250	314	702	37	451	446
Total	18,400	29.5	4.6	1.3	543,221	84,149	24,765	31,594	53,740	70,571

A visualization of the significant points contributing to the longitudinal stability of the aircraft are shown in Figure 34.

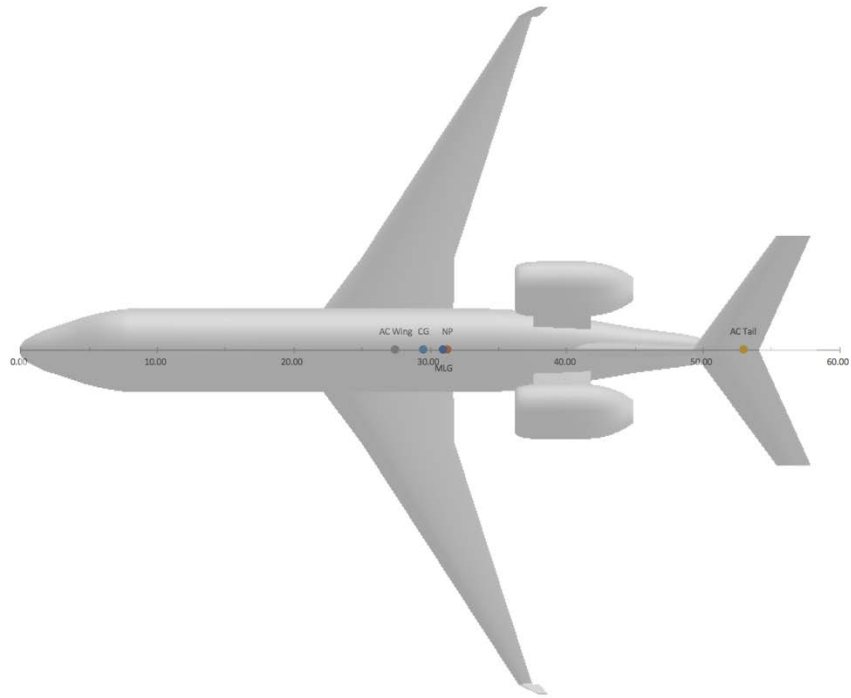


Figure 34. Top View of 8S Showing Relevant Points for Longitudinal Stability at MTOW

With the main landing gear mounted to the aft spar, the distance from the main landing gear to the wing aerodynamic center is fixed. Moving the wing causes large variations in the neutral point's position with relatively smaller changes to the center of gravity. Reducing static margin is achieved by moving the wing forward but is limited by the longitudinal tip over criteria. Figure 35 visualizes this relationship and shows why locating the wing at fuselage station 20 feet best satisfies both these constraints.

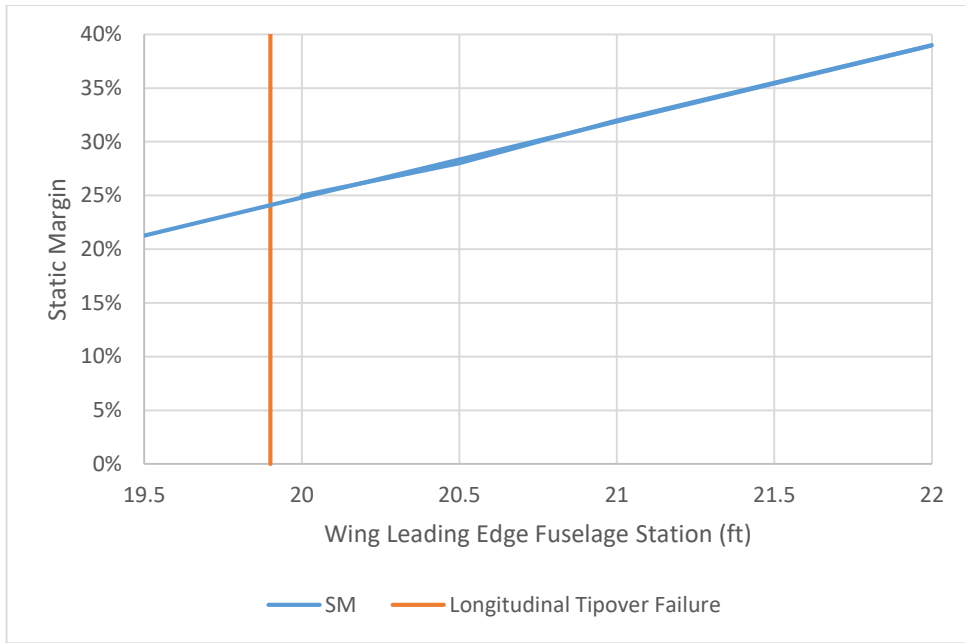


Figure 35. 8S Wing Position Constraints

The mission profile of the aircraft shifts throughout a flight, and this variation is captured the center of gravity excursion plot shown in Figure 36. The center of gravity envelope is forward of the neutral point, ensuring that longitudinal stability is maintained throughout the mission profile.

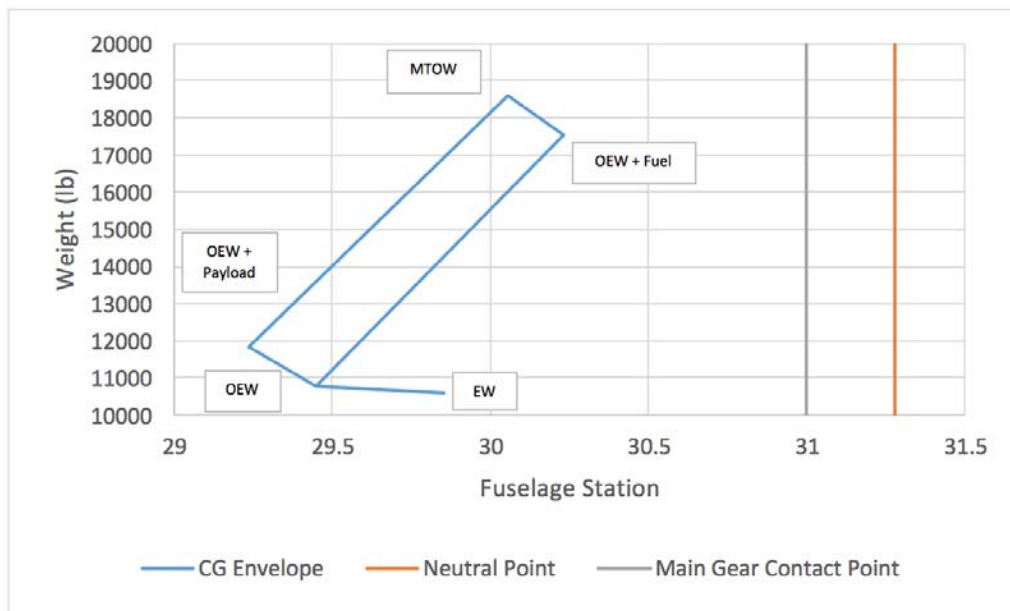


Figure 36. Profile of 8S Center of Gravity

6S Weight and Balance

A design goal of this project was a high degree of part commonality between these two aircraft. This was achieved largely in part by keeping the longitudinal stability of the aircraft in desirable positions with only minor modifications to the fuselage.

Five feet of fuselage was removed from the 8S to create the 6S with minimal impact to the fuselage layout. This could only be achieved by removing five feet of forward fuselage and shifting the wing back a small amount. Removing weight from the front of the plane destabilizes the plane so the neutral point must also be moved backward to maintain longitudinal stability. Figure 37 shows that this wing shift must be greater than 10 inches aft to satisfy the longitudinal tip over criteria. It was decided to move the wing 12 inches aft within the center section of the fuselage because this lined the leading edge on a fuselage spacer, making for a good attachment point. Unfortunately, the 6S experiences a bit more trim drag as a result but increases the commonality between the two.



Figure 37. Range of Static Margin and Longitudinal Tip Over Location for 6S Given Wing Shift with 5 feet of Forward Fuselage Removed

Removing a 5-foot fuselage section reduces the fuselage weight by 308 lb. Between this modification and moving the wing back 1 foot results in the new point mass layout shown in Figure 38.

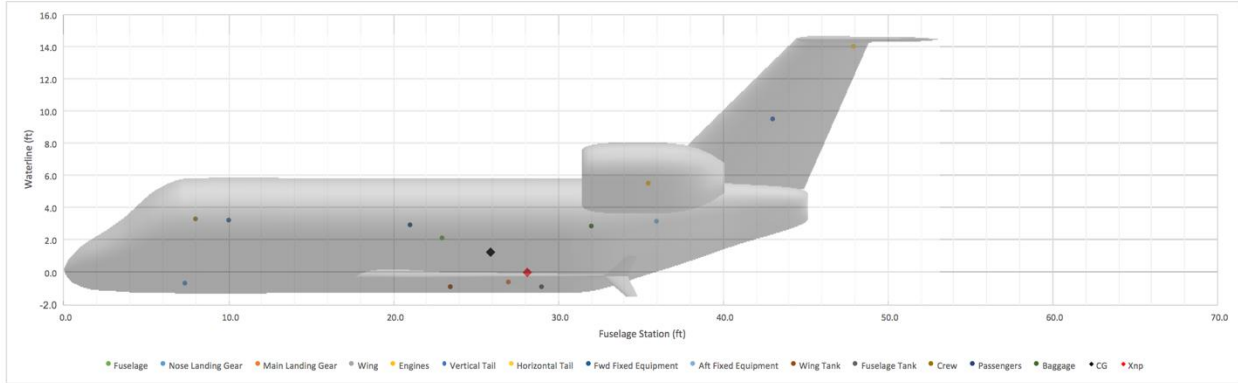


Figure 38. Point Mass Distribution of 6S at MTOW

A visualization of the significant points contributing to the longitudinal stability of the 6S aircraft are shown in Figure 39.



Figure 39. Top View of 6S Showing Relevant Points for Longitudinal Stability at MTOW

The mission profile of the aircraft shifts throughout a flight, and this variation is captured the center of gravity excursion plot shown in Figure 50. The center of gravity envelope is forward of the neutral point, ensuring that longitudinal stability is maintained throughout the mission profile.

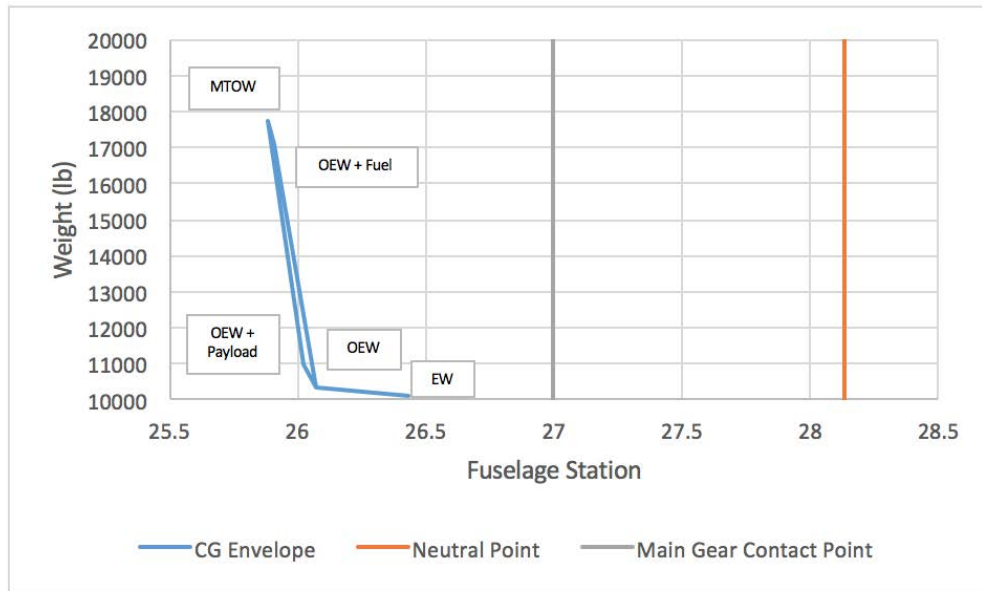


Figure 40. Profile of 6S Center of Gravity

Fuselage Manufacturing

The fuselage sections of the aircraft are broken up into 5 subassemblies all around 10 feet in length. These subassemblies are joined in the final assembly phase of the assembly line.

To keep the part commonality as high as possible, it was a design goal to use most of the same fuselage subassemblies for both the 8S and 6S. As explained in the previous section, the only modifications for the 6S fuselage is a 5-foot reduction from the 8S and a 1-foot shift of wing attach point in the center section. This reduction in fuselage subassembly can be seen when comparing Figure 41 and Figure 42.

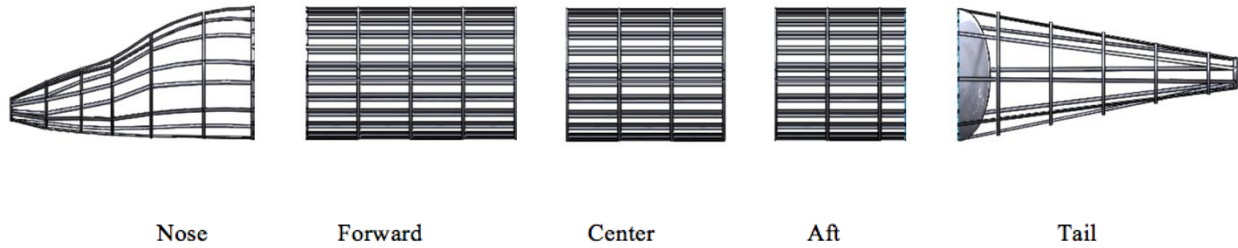


Figure 41. 8S Fuselage Subassemblies



Figure 42. 6S Fuselage Subassemblies

Besides this small modification in fuselage size and flight controller, which is discussed later, there are no other changes between the 8S and 6S. Excluding the engines of these two aircraft, the empty weights are 8,743 and 8,434 for the 8S and 6S, respectively. This means that 96% of the plane is similar by weight. This is not considering the 1 foot shift in wing position within the center fuselage, which is not a negligible change. This change will require new attach points and different shaped fuselage panels at a minimum. For conservatism, we'll assume this change will require 200 lb. of 8S material to be modified, bringing our part commonality percentage down to 94%, still well exceeding the 70% minimum desired by the RFP.

11. Stability and Control

Flight Dynamics

Once the wing and empennage have been designed, this geometry configuration was output from OpenVSP and fed into AVL with all the control surfaces with the primary aim of estimating the longitudinal and lateral-directional stability of Coronis 6 & 8. Since cruise is the lengthiest part of the mission profile, all following stability and control analysis was carried out with a Mach number of 0.75 and a C_L of 0.40 at

41,000 feet which result in an angle of attack for the both versions of Coronis as around 1.0° . Although it is understood by the designers that stability and control detailed analysis will require implementation during other critical phases of the mission profile such as takeoff and approach, the analysis during cruise was found to be sufficient for preliminary design purposes. Secondly, it was elemental in implementing a trim analysis for the minimum drag possible throughout most of the mission which consists of cruise predominantly. Therefore, the results derived in this section should only be taken as a use-case to demonstrate the correctness of the conceptual design choices made up to this point. The stability section is divided into two: longitudinal and lateral-directional stability for the 8- and 6-seater variants.

Trim Analysis

To determine the least drag configuration for the cruise portion of the mission, the horizontal stabilizer needs to be configured at such an angle of incidence that would balance the moment generated by the lift of the wing, making the elevator deflection zero. In other words, the horizontal tail will be at its cleanest and most streamlined condition during the longest part of the flight which will allow the designer to achieve the required cruise aerodynamic efficiency, hence the Mach number and range of the aircraft. The trim analysis was carried out in AVL software, distributed for free online by Massachusetts Institute of Technology.

Processing through several iterations of AVL calculations, the angle of incidence for the horizontal stabilizer of the 8-seater was determined to be 2.065° resulting in an elevator deflection of 0.006° , which is negligible. When the same process was carried out for the 6-seater, the angle of incidence of the horizontal tail was found to be 0.645° for an elevator deflection of -0.00228 , which is somewhat less than the 8-seater's. This is merely because the center of gravity of the 6-seater is closer to the neutral point (further aft) since the 6-seater is simply a 5-ft shortened version of Coronis 8 while the main wing is moved aft 1 feet. The following graphics (Figure 43 & Figure 44) demonstrate the lift force per local chord generated in the lifting surfaces and it is significant to observe the differences in the tail section between the variants.

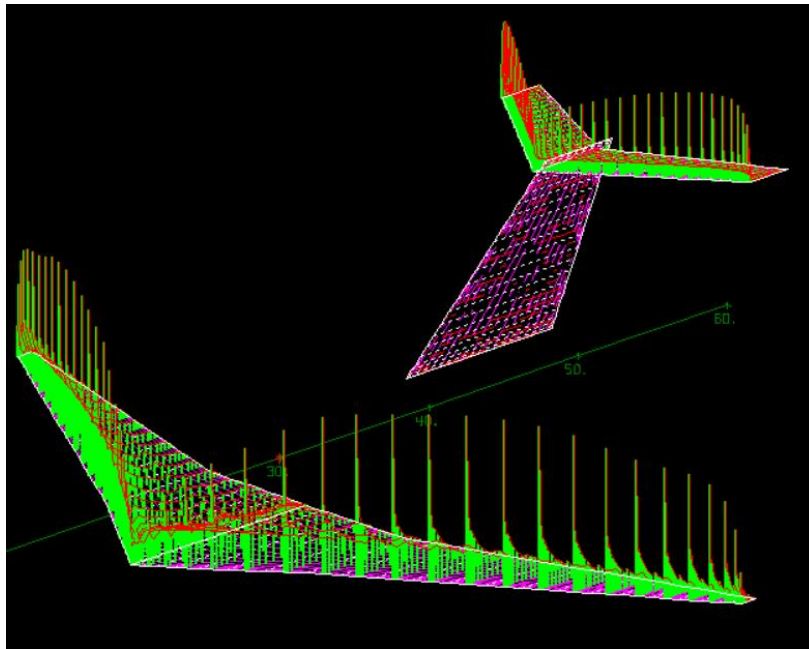


Figure 43. AVL Lift Distribution 8S in Cruise (CL = 0.40) at 41,000ft

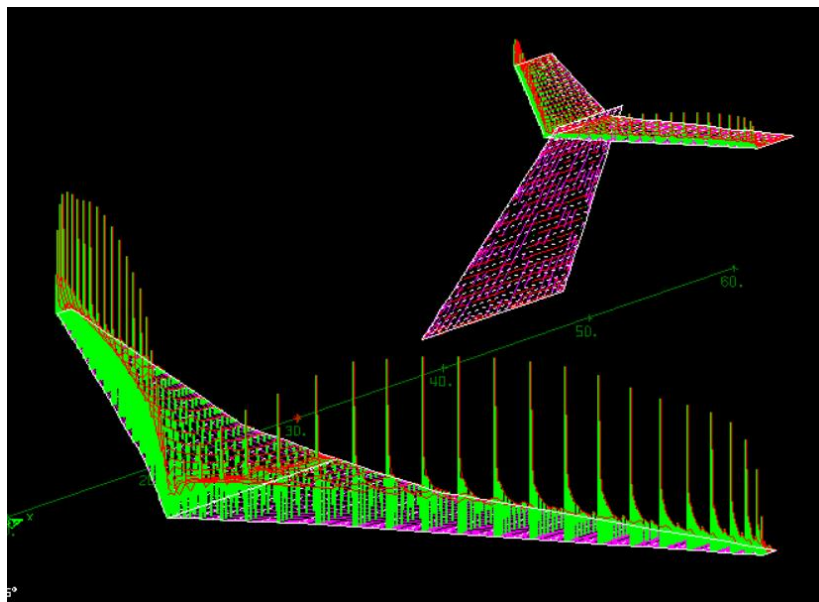


Figure 44. AVL Lift Distribution 6S in Cruise (CL = 0.40) at 41,000ft

As it can be clearly seen from the above figures, less lift is needed to be generated at the horizontal tail for the 6-seater to counteract the y-moment created by the lift acting through the center of pressure of the main wing. Since the horizontal stabilizer is at a lower angle of attack, lift induced drag is lower for the 6-seater compared to the 8-seater. In this sense, the former is considerably more aerodynamically efficient

compared to the latter. Although it is too early to say at this point in the design phase, the 6-seater is projected to have a higher cruise airspeed hence longer range and endurance.

The following Trefftz plots (Figure 45 & Figure 46) for the 8S and 6S, respectively, show the coefficient of lift distribution and downwash as a function of the span. These two plots are also obtained at cruise conditions with a prescribed C_L of 0.40. However, due to the difference in the trim characteristics of the variants, the angle of attack of the 8-seater is a little below 1° whereas the 6-seater is a minute amount above. This gives a higher overall C_L for the 6-seater which will increase lift-induced drag associated with this higher angle of attack. In addition, Coronis 8 also has higher downwash angles due to the increased lift which may cause higher interference drag with the fuselage downstream of the flow. With these considerations, the 6-seater may be less aerodynamically efficient in cruise, however, this may indeed be counteracted by the decreased angle of attack at the horizontal tail due to the lower incidence angle. To determine the actual result, either CFD for both airplanes should be executed or wind tunnel tests carried out.

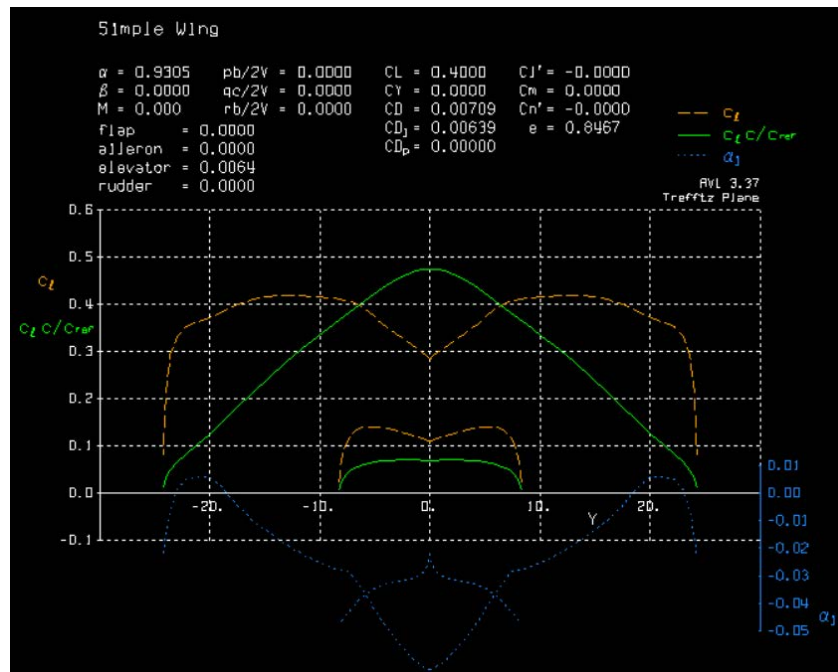


Figure 45. Trefftz Plot for 8S in Cruise ($C_L = 0.40$) at 41,000ft

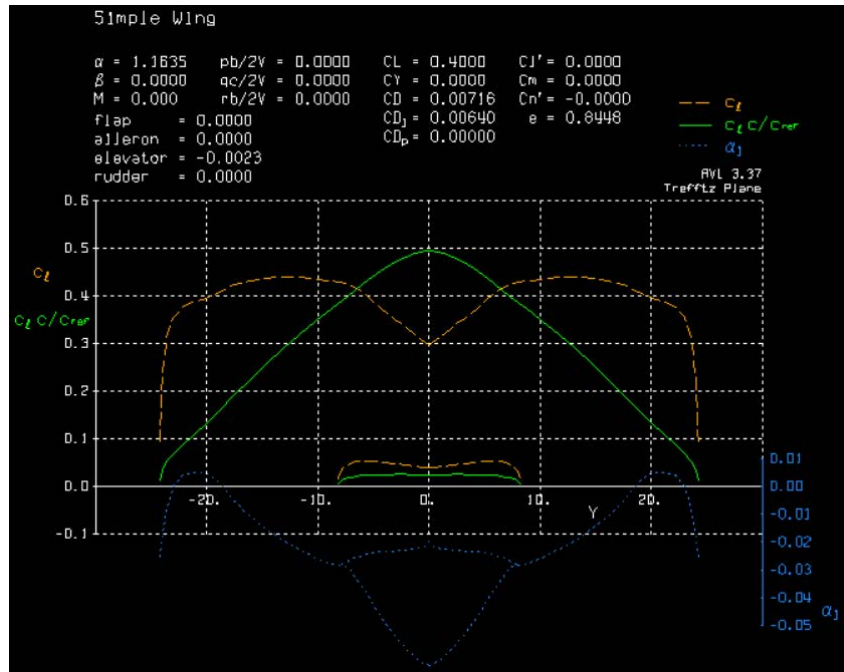


Figure 46. Trefftz Plot for 6S in Cruise ($C_L = 0.40$) at 41,000ft

Longitudinal Stability

With AVL, the location of the neutral points for both variants were determined and found to be in close agreement with the Class II Drag Polar Analysis presented earlier. The findings compared to the Class II method is presented in the following Table XXVI.

Table XXVI. Comparison of Neutral Point Determined with Class II Methods and AVL

	Neutral Point (ft)	
	Class II	AVL
Coronis 8	31.1	31.28
Coronis 6	26.1	27.12

The neutral point as calculated from the nose of the airplane and using the Class II approach has an error of -0.6% and -3.8% for the 8- and 6-seater variants, respectively. This close agreement between the methods confirm within an uncertainty that the processes used in longitudinal stability are likely not erroneous. As demonstrated by the center of gravity excursion diagram and the stated static margins, both of the variants are longitudinally stable throughout the mission profile given in the RFP.

The stability derivatives were used in deriving the longitudinal state-space matrices, A_{lon} and B_{lon} , which were then used in the Stability Augmentation System (SAS) that was implemented in the latter

sections of this paper. Using the approach outlined in Robert C. Nelson's *Flight Stability and Automatic Control*, the following matrices were directly taken for the controller implementation [13]:

$$A_{lon} = \begin{bmatrix} X_u & X_w & 0 & -g \\ Z_u & Z_w & u_0 & 0 \\ M_u + M_{\dot{w}}Z_u & M_w + M_{\dot{w}}Z_w & M_q + M_{\dot{w}}u_0 & 0 \\ 0 & 0 & 1 & 0 \end{bmatrix}$$

$$B_{lon} = \begin{bmatrix} X_{\delta} & X_{\delta_T} \\ Z_{\delta} & X_{\delta_T} \\ M_{\delta} + M_{\dot{w}}Z_{\delta} & M_{\delta_T} + M_{\dot{w}}Z_{\delta_T} \\ 0 & 0 \end{bmatrix}$$

The corresponding values have been determined using AVL and the resulting A and B matrices for the 8-seater are shown below. The second column of the B matrix was ignored since the given steady-state flight condition at cruise does not require the determination of the control derivatives with respect to a thrust input.

$$A_{lon,8} = \begin{bmatrix} -0.00399 & 0.034655 & 0 & -32.174 \\ -0.11663 & -0.56053 & 725.8 & 0 \\ 0.000182 & -0.00651 & -0.8381 & 0 \\ 0 & 0 & 1 & 0 \end{bmatrix}$$

$$B_{lon,8} = \begin{bmatrix} -0.01691 \\ -0.71234 \\ -0.13431 \\ 0 \end{bmatrix}$$

Similarly, the longitudinal A and B matrices for the 6-seater are shown below.

$$A_{lon,6} = \begin{bmatrix} -0.00397 & 0.038516 & 0 & -32.174 \\ -0.11471 & -0.57849 & 725.8 & 0 \\ 0.000395 & -0.01476 & -1.10363 & 0 \\ 0 & 0 & 1 & 0 \end{bmatrix}$$

$$B_{lon,6} = \begin{bmatrix} -0.00461 \\ -0.7358 \\ -0.18558 \\ 0 \end{bmatrix}$$

It should be noted here that comparing the longitudinal matrices for the 8- and 6-seater reveal the latter has more damping with respect to elements of the A matrix but less elevator control authority as indicated by the B matrix. The higher damping comes from the fact that the empennage and main wing possess the same size as for Coronis 8. For instance, the horizontal tail is just a little too large for the 6-seater which provides a higher damping hence stability once the aircraft is perturbed in the y-axis. However, on the other hand, the moment arm of the elevator with respect to the airplane c.g. is smaller in the 6-seater which makes the control derivatives with respect to an elevator deflection smaller. This will not prove to be a problem when the eigenvalues of the longitudinal modes are determined as can be seen in the latter sections of this paper.

Lateral-Directional Stability

A similar process to the longitudinal stability analysis was carried out for the lateral-directional dynamics using AVL. The following A and B matrices were directly taken from Nelson and were used in the implementation of a SAS controller to mainly damp the Dutch Roll mode of Coronis [13].

$$A_{lat} = \begin{bmatrix} Y_{\beta}/u_0 & Y_p/u_0 & -(1 - Y_r/u_0) & g \cos \theta_0 / u_0 \\ L_{\beta} & L_p & L_r & 0 \\ N_{\beta} & N_p & N_r & 0 \\ 0 & 1 & 0 & 0 \end{bmatrix}$$

$$B_{lat} = \begin{bmatrix} 0 & Y_{\delta_r}/u_0 \\ L_{\delta_a} & L_{\delta_r} \\ N_{\delta_a} & N_{\delta_r} \\ 0 & 0 \end{bmatrix}$$

The lateral-directional A and B matrices for the 8-seater variant is shown below.

$$A_{lat,8} = \begin{bmatrix} -0.04385 & 0.000172 & -0.99888 & 0.044329 \\ -12.9193 & -1.35209 & 0.362458 & 0 \\ 3.622603 & -0.01903 & -0.09445 & 0 \\ 0 & 1 & 0 & 0 \end{bmatrix}$$

$$B_{lat,8} = \begin{bmatrix} 0 & -0.00047 \\ 0.120998 & -0.06237 \\ 0.000599 & 0.045339 \\ 0 & 0 \end{bmatrix}$$

The same process was carried out for the 6-seater variant as well and shown below.

$$A_{lat,6} = \begin{bmatrix} -0.04539 & 0.000192 & -0.99885 & 0.044329 \\ -13.0532 & -1.36764 & 0.374807 & 0 \\ 4.748709 & -0.03046 & -0.12303 & 0 \\ 0 & 1 & 0 & 0 \end{bmatrix}$$

$$B_{lat,6} = \begin{bmatrix} 0 & -0.00049 \\ 0.122483 & -0.0627 \\ 0.000858 & 0.058859 \\ 0 & 0 \end{bmatrix}$$

Analogous to the longitudinal stability case, the 6-seater is damped a little more compared to Coronis 8 due to the proportionally larger empennage and wing as can be seen in the A matrix. Although the moment arm for the rudder is less, the rudder has slightly more control effectiveness as observed in the second column of the B matrix, which may be attributed to the larger size of the rudder control surface. In

addition, the aileron control effectiveness is also higher which is observed in the first column of the B matrix and naturally arises from the larger wing Coronis 8 main wing that was used for Coronis 6.

Stability Augmentation System

Now that the A and B matrices for both the longitudinal and lateral dynamics of the two aircraft have been found, a stability analysis can be performed. First, the longitudinal dynamics will be analyzed. The longitudinal dynamics consist of the phugoid and short-period mode. The phugoid mode is a lightly damped, long-period oscillation in pitch of the aircraft that results in the vehicle constantly exchanging airspeed for altitude and then altitude for airspeed. On the other hand, the short-period mode is typically a highly damped, short period oscillation in angle of attack in response to a sudden pitch input. After looking at the eigenvalues for the open-loop dynamics, it was discovered that the *Coronis 8S* met the level 1 flying qualities criteria without the addition of a stability augmentation system (SAS) while the *Coronis 6S* did not. Despite the *Coronis 8S* not needing a SAS to meet the longitudinal mode requirements, one was implemented anyway to fine-tune the short-period and phugoid response such that the longitudinal handling qualities would be very similar between the two designs. The controller design used to accomplish this is shown in Figure 47. Here, it can be seen that pitch rate and angle of attack feedback is used to modify the inputs from the pilots control. This allows the elevator deflection to be altered by the controller such that the phugoid and short-period modes have the desirable damping and natural frequency.

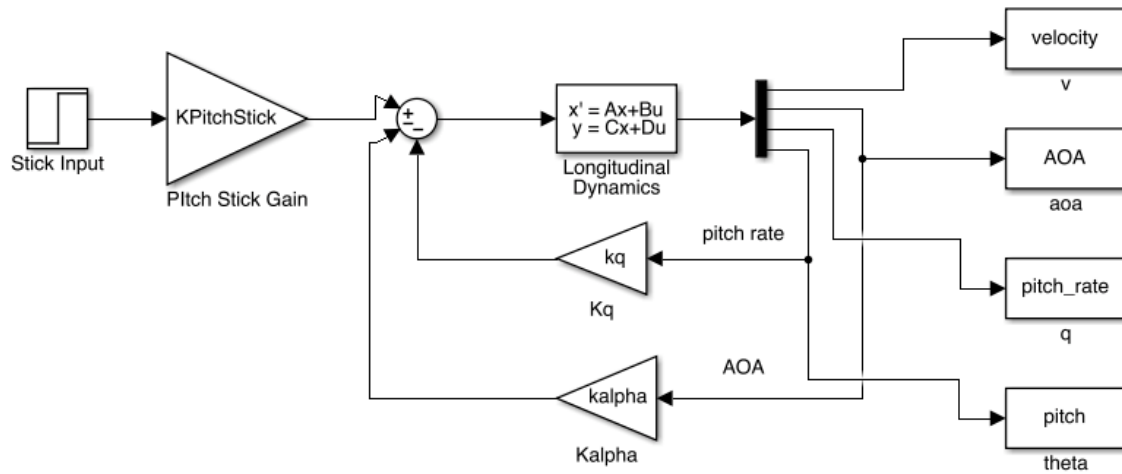


Figure 47. Simulink Model for Lateral-Directional SAS

Using MATLAB, the open-loop eigenvalues, damping, and natural frequency were computed for both the open-loop and closed-loop systems. These values were then compared in Table XXVII and

Table XXVIII below to see what effects the SAS had on the longitudinal dynamics of the 6S and 8S.

Table XXVII. Eigenvalue analysis for the longitudinal dynamics of the Coronis 6S

	Mode	Eigenvalues	ω_n (rad/s)	ζ
w/o SAS	Phugoid	-0.0019±0.074i	0.074	0.025
	Short-period	-0.84±3.26i	3.37	0.250
w/ SAS	Phugoid	-0.002±0.071i	0.071	0.027
	Short-period	-1.82±5.16i	5.47	0.332

Table XXVIII. Eigenvalue analysis for the longitudinal dynamics of the Coronis 8S

	Mode	Eigenvalues	ω_n (rad/s)	ζ
w/o SAS	Phugoid	-0.0017±0.073i	0.073	0.023
	Short-period	-0.70±2.17i	2.28	0.363
w/ SAS	Phugoid	-0.002±0.071i	0.071	0.027
	Short-period	-1.56±4.39i	4.66	0.335

The gains used in the SAS for both aircraft are shown in Table XXIX below. These gains were adjusted such that the level one flying qualities given by Cooper and Harper would be met.

Table XXIX. Gains used for the longitudinal SAS.

Model	k_α	k_q
Coronis 6S	-0.13	-10.0
Coronis 8S	-0.16	-12.0

These level one flying qualities criteria for the short-period and phugoid mode along with the actual values for the aircraft after implementing the SAS are shown in Table XXX below. From these results, it is clear that both aircraft have level one flying qualities for both longitudinal modes.

Table XXX. Longitudinal modes requirements and results.

Short Period Mode	ω_n^2/n_α	ζ
Level 1 Requirement	$0.085 < \omega_n < 3.6$	$0.3 < \zeta < 2.0$
Coronis 6	2.28	0.332
Coronis 8	1.66	0.335

Phugoid Mode	ζ
Level 1	No requirement
Coronis 6	0.03
Coronis 8	0.03

Now that the SAS has been successfully implemented to improve the longitudinal dynamics of the aircraft, it is now time to design a lateral SAS to improve the lateral dynamics of the aircraft. The lateral-directional modes consist spiral, roll, and Dutch-roll modes. The spiral mode captures the long-term behavior of the bank angle of an aircraft when displaced from a wings-level attitude. If this mode is stable, the wings will return to a level bank angle. If unstable, the bank angle will diverge away into a higher and higher bank angle. This mode typically has either a small negative or positive value for the damping. The roll modes consist of the aircraft's short-term response to a roll command. High damping indicates very abrupt and

crisp responses to an input while low damping will result in a softer and gentler response. In the case of business jet aircraft, high damping for this mode is not desirable because of the abrupt handling quality that it would create. Passengers prefer smooth transitions in bank angles rather than the precise and sharp roll responses that would be expected from a military jet. Finally, there is the Dutch-roll mode. This mode consists of an undesirable coupling between the yawing and rolling motion of the aircraft. This mode tends to cause passenger discomfort in the form of nausea and thus is very important that it be properly damped by the SAS. The controller design used to tune the behavior of these modes is shown in Figure 48 below. In this controller, yaw rate is used as feedback for the rudder. This yaw rate is first passed through a high-pass filter to remove the steady-state yaw rate.

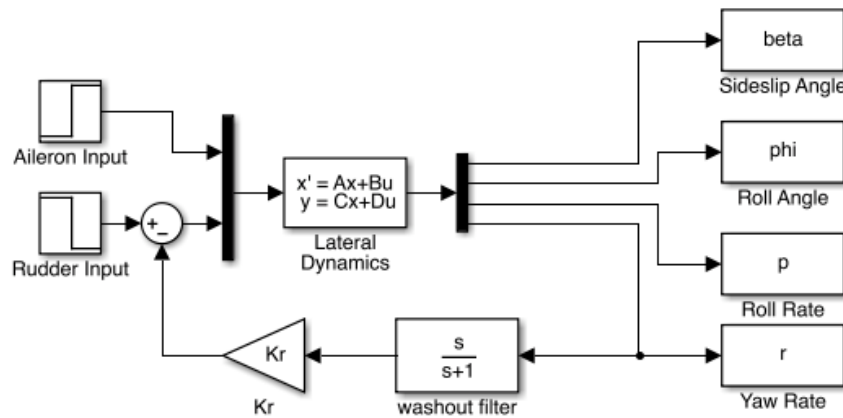


Figure 48. Simulink Model for Lateral-Directional SAS

Using MATLAB, the open-loop eigenvalues, damping, and natural frequency were computed for both the open-loop and closed-loop systems. These values were then compared in below to see what effects the SAS had on the lateral dynamics of the 6S and 8S.

Table XXXI. Eigenvalue analysis for the lateral dynamics of the Coronis 6S

	Mode	Eigenvalues	ω_n (rad/s)	ζ
w/o SAS	Spiral	1.03×10^{-3}	1.03×10^{-3}	-1.00
	Roll	-1.51	1.51	1.00
	Dutch Roll	$-0.0138 \pm 1.96i$	2.23	6.21×10^{-3}
w/ SAS	Spiral	0.001	0.001	-1.00
	Roll	-1.48	1.48	1.00
	Dutch Roll	$-0.230 \pm 2.08i$	2.09	0.110

Table XXXII. Eigenvalue analysis for the lateral dynamics of the Coronis 8S.

	Mode	Eigenvalues	ω (rad/s)	ζ
w/o SAS	Spiral	7.20×10^{-4}	7.20×10^{-4}	-1.00
	Roll	-1.50	1.50	1.00
	Dutch Roll	$.00195 \pm 1.96i$	1.96	-9.9×10^{-4}
w/ SAS	Spiral	6.94×10^{-4}	6.94×10^{-4}	-1.00
	Roll	-1.45	1.45	1.00
	Dutch Roll	$-0.193 \pm 1.80i$	1.81	0.106

The gains used in the lateral SAS for both aircraft are shown in Table XXXIII below. These gains were adjusted such that the level one flying qualities given by Cooper and Harper would be met.

Table XXXIII. Gains used for the lateral SAS.

Model	k_r
Coronis 6S	10.0
Coronis 8S	13.0

These level one flying qualities criteria for the roll, spiral, and Dutch-roll modes along with the actual values for the aircraft after implementing the SAS are shown in Table XXXIV below. From these results, it is clear that both aircraft have level one flying qualities for all three lateral-directional modes.

Table XXXIV. Lateral-directional modes requirements and results.

Roll Mode	Time Constant (sec)
Level 1 Requirement	≤ 1.4
Coronis 6	0.68
Coronis 8	0.69

Spiral Mode	Doubling Time (sec)
Level 1 Requirement	None
Coronis 6	693
Coronis 8	998

Dutch Roll Mode	ζ	ω_n (rad/s)	$\zeta\omega_n$ (rad/s)
Level 1 Requirement	>0.052	>0.4	>0.15
Coronis 6	0.110	2.09	0.23
Coronis 8	0.106	1.81	0.19

While this SAS design was only done for the cruising configuration, given more time this analysis would be extended to all phases of flight. The controller would then adapt to have the appropriate gains to achieve the desired handling qualities for each respective phase of flight. The process in doing this would be the same as outlined above.

From the addition of the SAS for both the longitudinal and lateral-direction modes, the handling qualities of the Coronis 6S and Coronis 8S have been improved such that the aircraft in the cruising configuration meets the Cooper and Harper level one handling qualities for business-jet type aircraft. In addition to this, the controllers have been designed such that the damping of the different modes for both aircraft are almost identical. This ensures that pilots who operate both the 6S and 8S variants will experience a seamless transition in handling qualities. This increases the operational safety and appeal of the *Coronis* lineup.

12. Subsystems

Hydraulics

The hydraulic subsystem for the Coronis 6 and Coronis 8 is the primary subsystem for aircraft control. The front and main gear are hydraulically actuated, along with the rudder, elevators, ailerons, and flaps. Pressure for the system is provided by three pumps, one per engine and one on the APU; each engine has an accessory gearbox to extract mechanical power for the hydraulic pump. A high-level schematic of the system is presented in Figure 49. This high-level schematic is common to both aircraft; the same actuators and pumps are used for both models. For a smaller footprint, higher-pressure lines at 5,000 psi

are implemented to reduce required pipe diameters. While the flight controls are hydraulically actuated, control is achieved through an electric fly-by-wire system, also reducing weight and allowing implementation of stability and control augmentation systems.

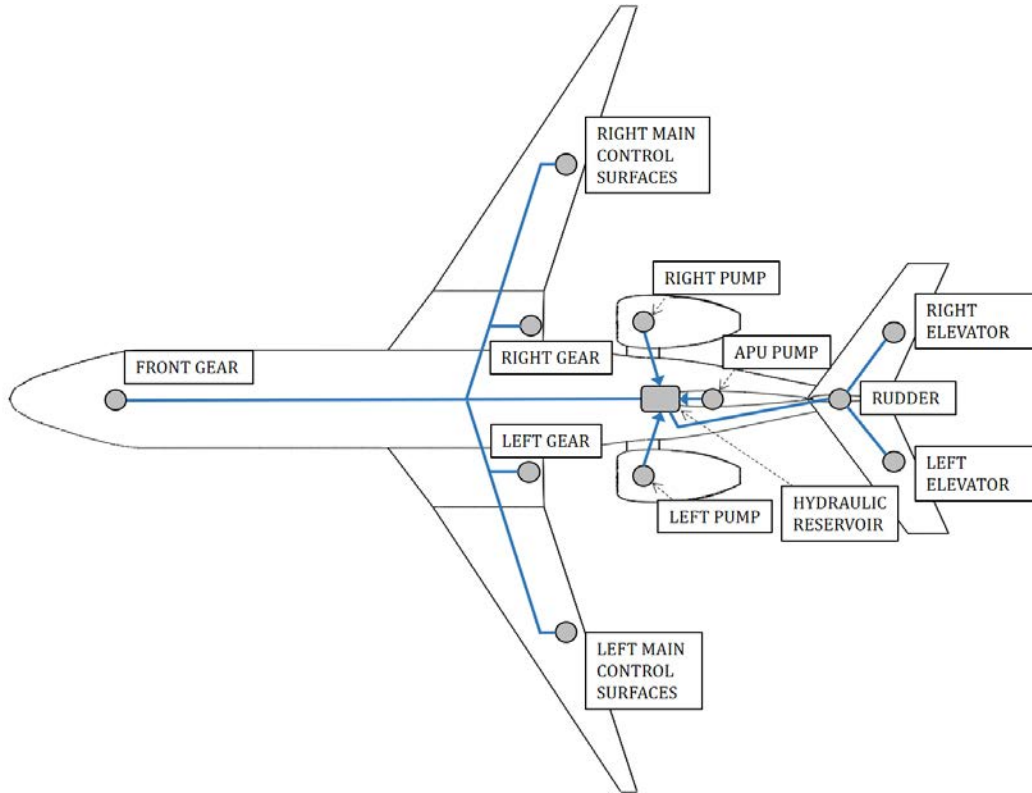


Figure 49. Hydraulic Subsystem Schematic for 8S and 6S

Electric

The electric subsystem for the Coronis 6 and Coronis 8 is also common to both aircraft, featuring three generators: one on each engine and one on the APU. Each engine has an accessory gearbox to extract mechanical power for the generator. These generators output a voltage of 115 VAC with a frequency of 400 Hz; the main electrical conduits run from these generators in the rear of the aircraft to both the front and rear power control units. These units function to frequency-convert the 115 VAC power to 60 Hz for passengers' electronic devices, and convert to 28 VDC for the batteries and avionics. A large, high-

amperage battery is located in the rear of the aircraft, used for APU starting; the main battery, used for backup power, is located in the front of the aircraft. A high-level overview of the electric subsystem is presented in Figure 50.

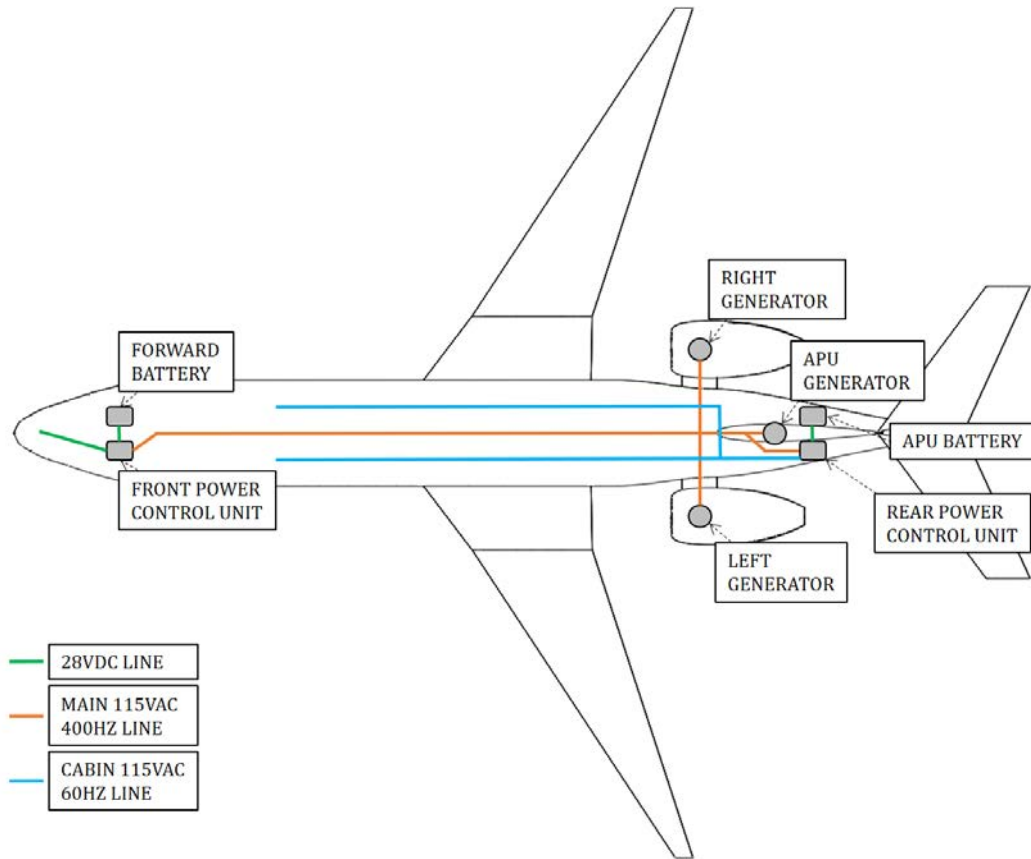


Figure 50. Electric Subsystem Schematic for 8S and 6S

Fuel

The Coronis 6 and Coronis 8 both feature wing fuel tanks and a single fuselage tank to meet fuel requirements. To properly regulate the usage and flow of fuel, a central fuel hopper is utilized, allowing for crossflow between tanks to help adjust the center of gravity in flight. This central fuel hopper feeds fuel to the two engines and the APU in the rear of the aircraft. A high-level overview of the fuel subsystem is presented in Figure 51. For refueling, both over-wing gravity refueling and pressure refueling are offered.

Gravity refueling ports are located on top of each wing to directly fill the wing tanks; through this method, power is required to fill the fuselage tank. Pressure refueling is accomplished using the fuel hopper to distribute fuel quickly to all three fuel tanks.

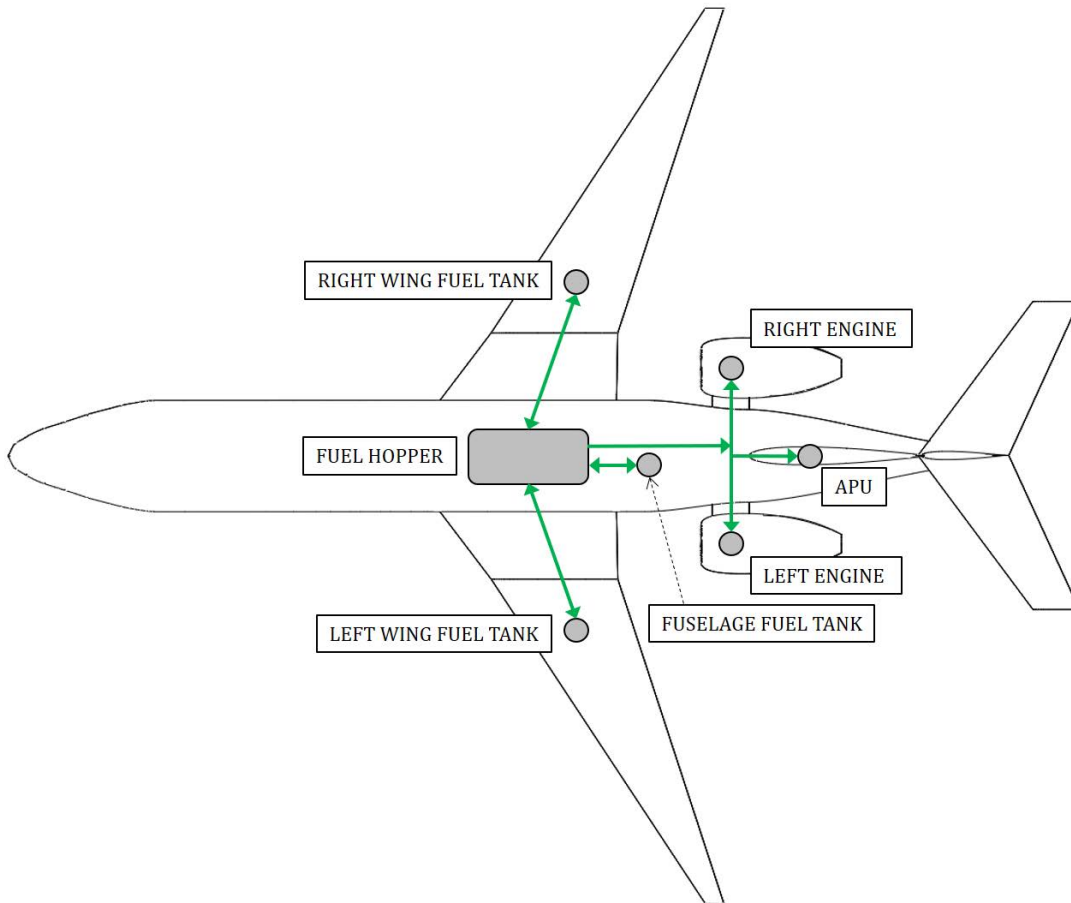


Figure 51. Fuel Subsystem Schematic for 8S and 6S

Pneumatic

Common to both the Coronis 6 and Coronis 8, the pneumatic subsystem primarily functions to start the engines using bleed air from the APU. It also provides hot air for de-icing and ice protection, and conditioned air for passenger comfort. A high-level overview of the pneumatic system is presented in Figure 52.

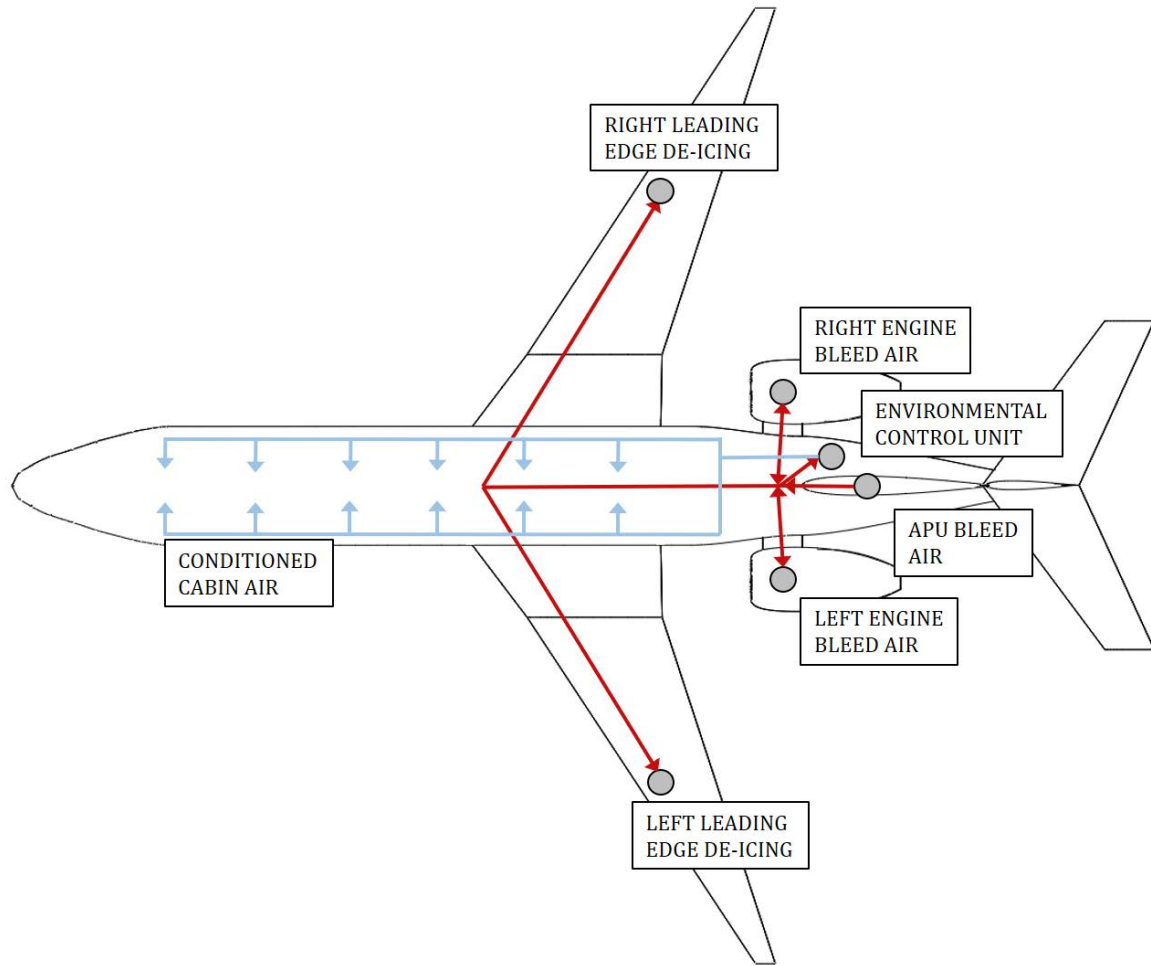


Figure 52. Pneumatic Subsystem Schematic for 8S and 6S

13. Interior

Cockpit/Flight Deck Design

Figure 53 below shows a theoretical flight deck layout for the Coronis family of aircraft. The Garmin G5000 flight deck solution was chosen as a likely candidate for a single integrated avionics solution due to its excellent reputation as a seamless and easy to use system utilized by both single pilot and crew flown business jet aircraft.



Figure 53. Avionics

Cabin Design

Using Roskam's Airplane Design Part III, Figures 3.45 and 3.52 [14], cabin design values were estimated. A width of 30 inches was determined for the primary entrance, providing comfortable entry for average persons; this also determined the width of the lavatory section. For standard Coronis 6 and Coronis 8 layouts, the galley is opposite the entrance; therefore, it also has a width of 30 inches. For luxurious seating, a seat width of 20 inches was chosen, with two inch armrests and 22 inches of seat depth. A seat pitch of 41 inches was selected for maximum comfort in the Economy layout. Aisles feature a 12.3-inch width at their smallest; 16.3 inches is typical. Differences between the Coronis 6 and Coronis 8 in the cabin are mainly in the seating and cargo sections; overall, the Coronis 6 reduces length by 5 feet. Of this, 43 inches comes from reduction in the seating section from removing one row of seats, and 17 inches comes out of the cargo section. These cabin design parameters are presented in Table XXXV.

Table XXXV. Cabin design parameters.

Parameter	Value
Entrance Width (in)	30
Galley Width (standard) (in)	30
Galley Width (extended) (in)	50
Lavatory Width (in)	30
Seat Width (in)	20
Seat Depth (in)	22
Seat Pitch (in)	41
Armrest Width (in)	2
Aisle Width (typical) (in)	16.3
Cabin Length (Coronis 6) (ft)	23.75
Cabin Length (Coronis 8) (ft)	28.75

Cabin Options

Both the Coronis 6 and Coronis 8 offer five options for the interior layout. Each have a basic Economy layout, which fits in as many forward-facing seats as possible while maintaining luxurious wide seats and ample legroom. A more luxurious option, the Executive layout, removes 3 seats in favor of having two pairs of seats facing one another with a table between each, and includes an extended galley and couch capable of comfortably seating three individuals. Two utilitarian options are also available; these are the Utility and Medical layouts. Targeted more for corporate or government use, or for individuals who wish to utilize the short take-off and landing capabilities to go to more extreme environments, these layouts offer tie-down rails along the floor and smaller, lightweight chairs which can be attached or removed depending on the owner's desire. The Utility layout's cabin is entirely filled with rails; the Medical layout includes both built-in cabinets and counter space for medical equipment, and a built-in medical cot for patient transport.

Economy Layout

The Economy layout is the basic layout for both aircraft; the Coronis 6 has three rows of wide, plush leather seats, and the Coronis 8 adds an extra row of seating. Each seat has an articulating flat-screen

LED TV for entertainment, and outlets for powering passengers' various personal electronic devices. The lavatory features a modern vanity, constructed with rosewood accents and copper. The galley, too, is constructed with rosewood accents and copper; it provides cabinet space for any passenger's libationary or culinary desires. The cargo hold is accessible through the lavatory and externally. CAD renders for both the Coronis 6 and Coronis 8 interior are presented below in Figure 54 and Figure 55.

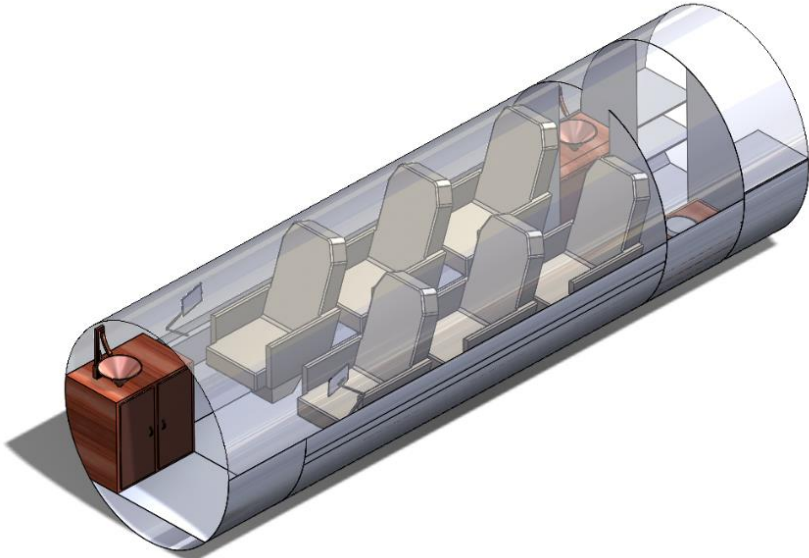


Figure 54. Economy Layout for the Coronis 6.

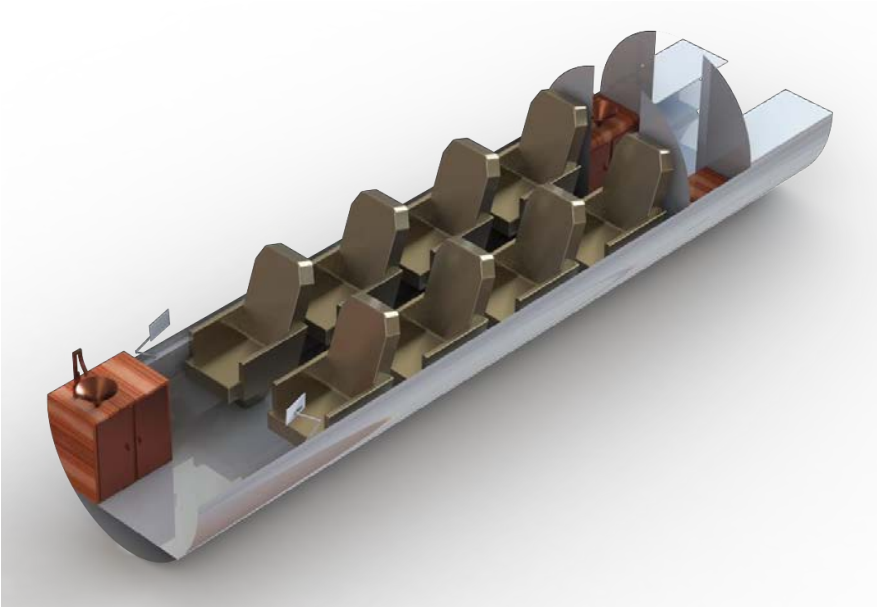


Figure 55. Economy Layout for the Coronis 8

Executive Layout

The Executive layout is the most luxurious interior layout offered for the Coronis 6 and the Coronis 8. The option for the Coronis 6 offers two pairs of seats facing one another with a stowable table between each, and a small couch. The option for the Coronis 8 also offers two pairs of seats facing one another with a stowable table between each pair, a fifth forward-facing seat, and a couch capable of comfortably seating three; it is presented below in Figure 56. The Executive layout also extends the galley from 30 inches in length to 50 inches in both models; it is constructed of rosewood and copper, and it provides extra cabinet space for any passenger's libationary or culinary desires. Like the Economy layout, each seat has an articulating flat-screen LED TV for entertainment, and outlets for powering passengers' various personal electronic devices.

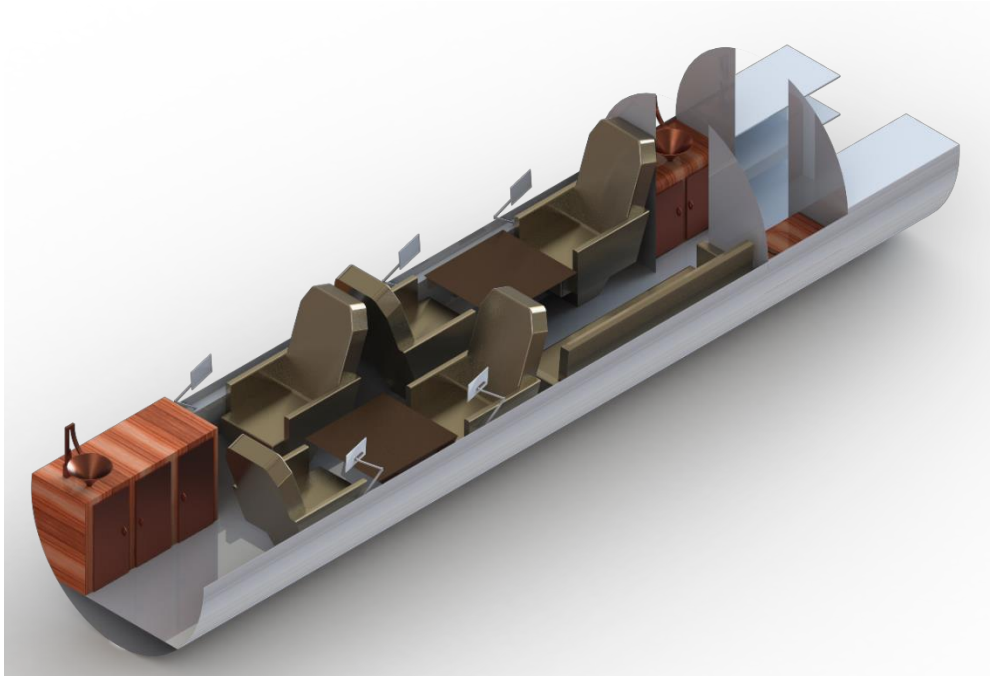


Figure 56. Executive Layout for the Coronis 8.

Utility Layout

The Utility layout is completely customizable for the needs of the owner. The only fixed equipment in the cabin is the galley and lavatory; the rest of the cabin consists of open space, with rails of tie-downs

running along the cabin floor. This variant of the Coronis 6 and Coronis 8 ships with six and eight small, lightweight, yet still comfortable chairs respectively, and three and four 28 inch by 28 inch pallets respectively, for external packing. The Coronis 8 variant is presented in Figure 57, along with one of the chairs and one of the pallets. This layout features durable, ruggedized interior components which can take a beating, and be cleaned with a hose; there's no need for the owner to worry about dirt and grime when taking the Coronis 6 or Coronis 8 out for a weekend hunting expedition. For our government contractors, this makes the jet extremely useful in allowing quick turnarounds on preparing the cabin for the next mission.

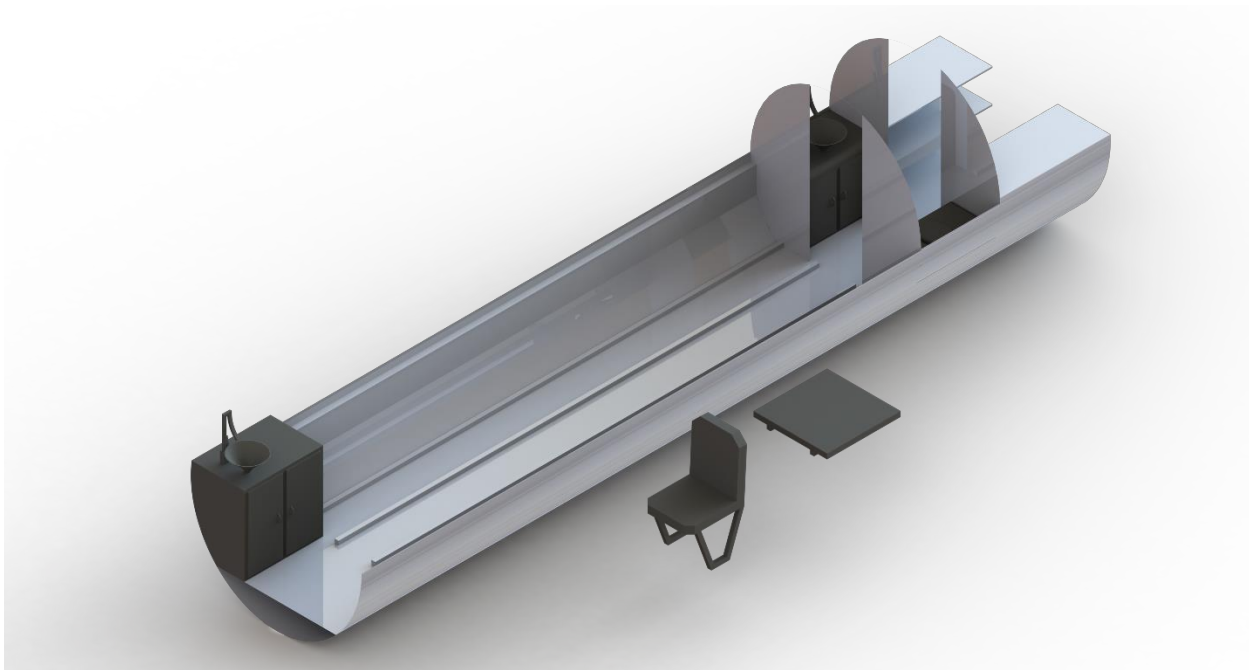


Figure 57. Utility Layout for the Coronis 8.

Medical Layout

The Medical layout takes the same base as the Utility layout, and adds both built-in cabinets and counter space for medical equipment, and a built-in medical cot for patient transport. It features the same durable, ruggedized interior components, making it extremely easy to clean and prepare the cabin for the next patients in need of quick air transport to a safer location with medical assistance. It also has the same

tie-down rails along the floor, and small, lightweight, yet comfortable chairs. The Coronis 6 and Coronis 8 come with two and four of these chairs, respectively, for placement wherever the owner desires; an example of the Coronis 8 layout is presented in Figure 58. This layout targets mostly government agencies in need of a way to quickly evacuate individuals from remote locations; with the short takeoff and landing capabilities of the jet, the Coronis 6 and Coronis 8 make perfect medevac aircraft.

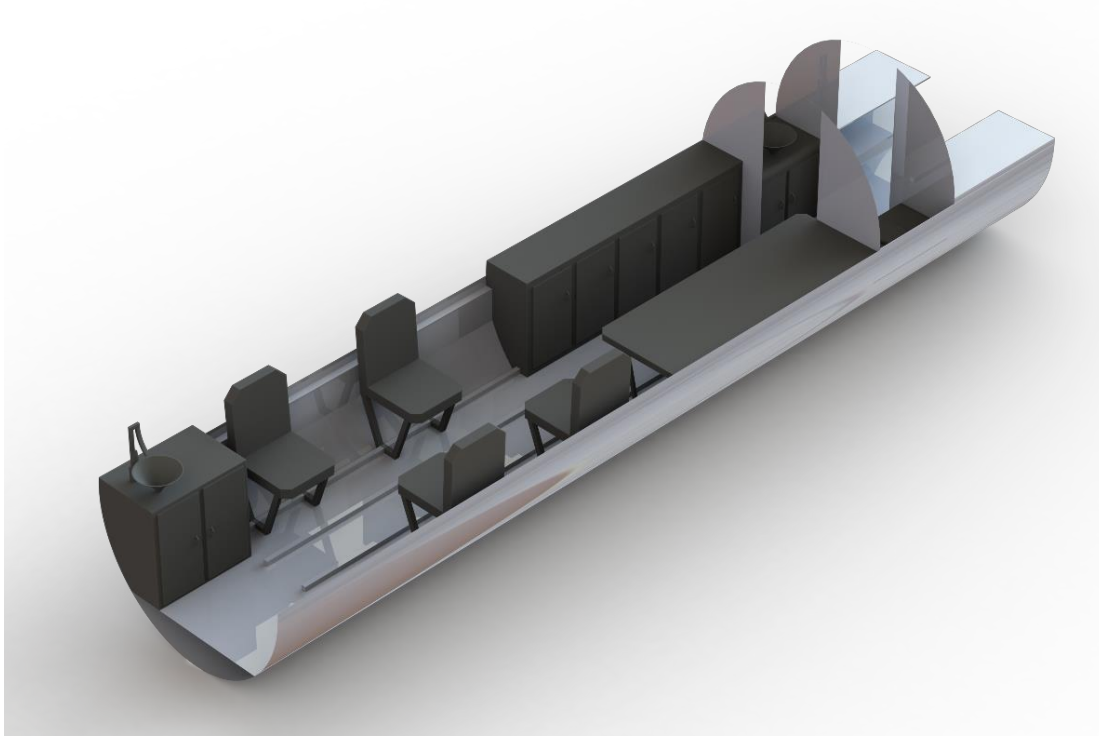


Figure 58. Medical Layout for the Coronis 8.

14. Cost and Finances

Eastlake Cost Estimation Model

In determining the economics for the business proposal presented for the two variants of the Coronis aircraft, a highly-modified version of DAPCA-IV, the Eastlake aircraft cost estimation model was used [15]. This financial model was divided into two sections which outline the procedures involved in

estimating the non-recurring and operational costs associated with the initial phases of the airplane's lifetime.

Developmental Costs

The developmental part of the financial model utilizes the following major preliminary design parameters of the aircraft: structural empty weight and maximum level airspeed, with correction factors applied such as the cost associated with power plants, standard airworthiness certification (CFR Parts 23 & 25), avionics, and complex manufacturing technologies such as the implementation of pressurization, tapered wings, and complex flap systems. Moreover, an important human factor parameter is also included, namely the Quantity Discount Factor (QDF), which considers the learning curve that the engineers, technicians, and mechanics experience throughout the developmental process, reducing costs and increasing manufacturing times exponentially.

The total developmental cost was divided into two: certification cost (fixed) and manufacturing & quality control cost (variable). The certification cost can be further divided into its subparts which are expressed in the following expression:

$$C_{CERT} = C_{ENG} + C_{DEV} + C_{FT} + C_{TOOL} \quad (19)$$

where C_{CERT} is the certification cost, C_{ENG} is the engineering cost, C_{DEV} is the development support cost, C_{FT} is the flight testing cost, and C_{TOOL} is the tooling cost. The variable costs were calculated in the following way:

$$C_{VAR} = C_{MFG} + C_{QC} + C_{MAT} + C_{PP} + C_{AV} \quad (20)$$

where C_{VAR} is the variable cost, C_{MFG} is the manufacturing labor cost, C_{QC} is the quality control cost, C_{MAT} is the materials/equipment cost, C_{PP} is the power plant cost, and C_{AV} is the avionics cost. The total developmental cost of the aircraft then becomes:

$$C_{TOT} = C_{CERT} + C_{VAR} + C_{INS} \quad (21)$$

where C_{TOT} is the total developmental cost of the aircraft and C_{INS} is the manufacturer's liability insurance. The following pie-chart (Figure 59) summarizes the developmental cost division for both variants of Coronis as the fixed-costs are equal.

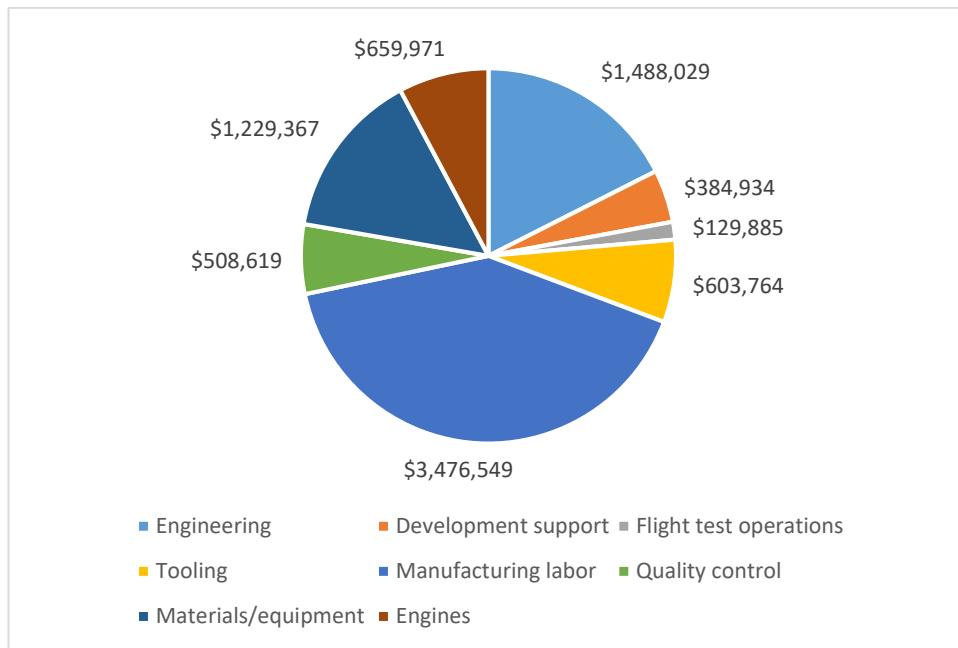


Figure 59. Breakdown of 8S Cost Based on Sales of 200 Aircraft over 5 Years

If the above procedure is carried out to determine the total cost of the program, it would be a conservative estimate of what the whole design, manufacturing, and flight testing would in reality come out to be. In order to account for the learning curve that engineers, mechanics, and technicians go through as the design process progresses, the Quantity Discount Factor was introduced using the following equation:

$$QDF = (F_{EXP})^{1.4427 \ln N} \quad (22)$$

where QDF is the Quantity Discount Factor, F_{EXP} is the experience effectiveness, and N is the number of aircraft units produced. For the Coronis Light Jet Aircraft program, F_{EXP} was assumed to be 0.85 which is neither conservative nor optimistic. A conservative value such as 0.80 was not chosen as it is assumed that the aircraft design in question implements technologies that are already in the market and have been utilized for at least 10 years or more. Applying QDF to the final total developmental cost decreased the cost of both Coronis 8 & 6 by as much as %15. The second variable in the equation requires the number of aircraft to be produced and sold over a period of 5 years, which was calculated utilizing a break-even analysis as outlined by the Eastlake Model. The following relation was used:

$$N = \frac{\text{total fixed cost}}{\text{unit sales price} - \text{unit variable cost}} \quad (23)$$

from which a trade study was conducted to determine a reasonable decision on how many units of aircraft was needed to be produced in the first 5 years. The following Figure 60 demonstrates the results of the trade study.

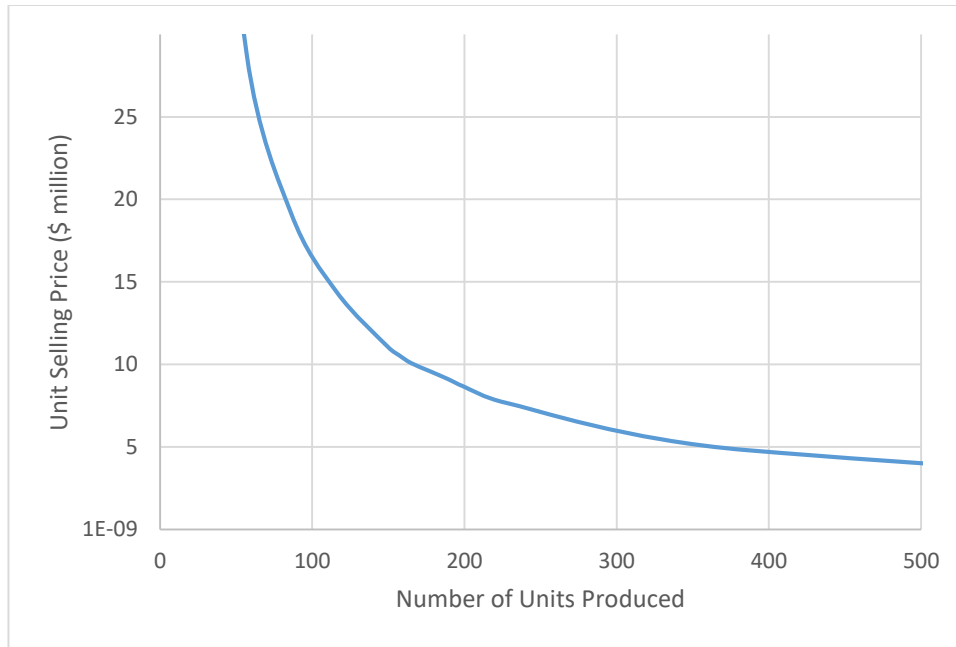


Figure 60. Minimum Selling Price of 8S over 5 Years of Production to Break Even

As was expected, the break-even trade study concludes that the unit cost to produce the Coronis decreases exponentially as the number of units sold increases. In order to fit the market trend of similar aircraft that are already in production, the number of units to be produced over a period of 5 years was selected to be 200, equally divided between the 8-seater and 6-seater versions i.e. 100 aircraft to be produced per variant. This approach works since there is a significant amount of part commonality between the two models which allows the designers to assume negligible the certification cost that would be present if the 6-seater was designed separately with little part commonality. These financial analysis decisions are summarized in Table XXXVI below.

Table XXXVI. Summary of financial decisions.

Variant	# Produced (0-5 Years)	Fixed+Variable Cost (\$)	Selling Price (\$)
Coronis 8	100	9,595,609	9,636,048
Coronis 6	100	9,518,742	8,566,868

It is important to note here that the selling price of the 6-seater is 10% less than the total cost to produce one aircraft. This is simply because if 100 of the Coronis 6 is produced and sold in the first 5 years,

the executives of the company expect to break-even. In contrast, the 8-seater will be on the market for \$1M more than the break-even price for 100 aircraft sold. This is mainly a marketing and business decision to “create” a financial difference between the two variants of Coronis, giving the customer the impression of a significant upgrade between the two aircraft. If the break-even minimum selling price for both of the aircraft are chosen to be marketed as is, the difference between their selling price will be approximately \$77,000 which does not give the 6-seater variant a competitive edge in the market.

The Coronis design group does not project to make significant profit in the first 5 years, which is planned to be the “break-even period” to pay the fixed-costs associated with the design process. After the first 5 years is over, the only financial cost to the company will be the variable cost associated with producing each aircraft since the certification cost will be paid by the first 200 aircraft sold. With these predictions, the course succeeding the initial 5-year period will be the prime driver of the profits generated from the Coronis aircraft. With the fixed-costs disappearing into non-existence, the following predictions summarized in Figure 61 are expected to hold.



Figure 61. Aircraft Pricing Based on Sales of 200 Aircraft over 5 Years

Operational Costs

Carrying out a similar procedure as outlined in the Eastlake Aircraft Cost Estimation Model, the annual operational cost for the Coronis aircraft is determined [15]. The total operational cost once the aircraft purchased is given by the following relation.

$$C_{YEAR} = C_{AP} + C_{STOR} + C_{FUEL} + C_{INS} + C_{INSP} + C_{OVER} + C_{LOAN} \quad (24)$$

where C_{YEAR} is the total yearly operational cost, C_{AP} is the maintenance cost, C_{STOR} is the storage cost, C_{FUEL} is the fuel cost, C_{INS} is the insurance cost, C_{INSP} is the inspection cost, C_{OVER} is the engine overhaul fund, and C_{LOAN} is the loan payment where each of these parameters are calculated in an annual basis. The major operational cost variables are summarized in Table XXXVI below.

Table XXXVII. Summary of operational costs.

Parameter	Value
Flight Hours/Year	500
Annual Storage Cost	\$18,000
Cruise Gallons/Hour	140
Annual Insurance Cost	\$15,000
Annual Engine Overhaul Fund	\$7500
Crew Salary/Hour	\$150
Annual Loan Payment	\$0

It is significant to note here that it was assumed that the buyer of the aircraft would not acquire a loan to purchase the aircraft. This operational cost parameter was valued as such since it is quite variable and hard to predict: depends heavily on each customer and the loan rates available (if an annual loan payment is present, one should expect an increase in the operational costs by 100% or more).

Secondly, the operational costs of the 8- and 6-seater variants are assumed to be quite similar. Since the constraining variant in the preliminary design process was the heavier and larger Coronis 8, the flight performance values were calculated accordingly. Since the only two differences between the variants would

be a slight reduction in fuel consumption for the 6-seater in cruise and decreased loan payment due to its selling price, the operational costs were assumed to be similar between Coronis 6 & 8. The following Figure 62 is representative of the operational cost division for the two variants which puts the total cost at approximately \$650,000 per aircraft per year.

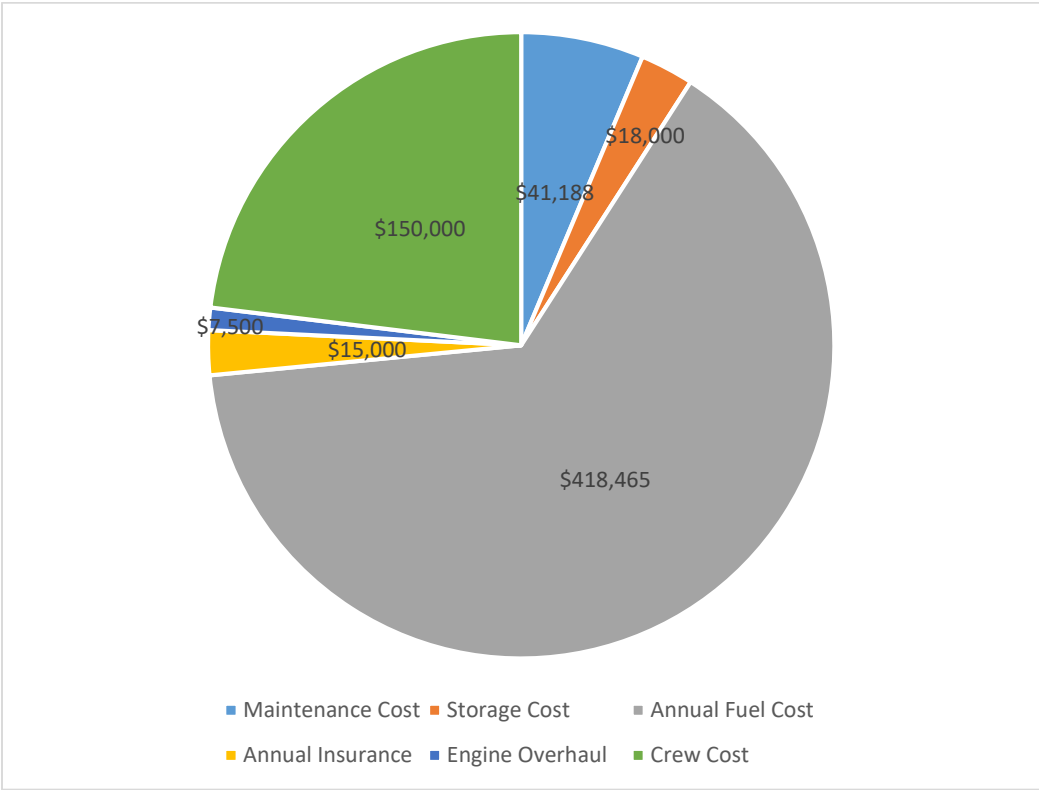


Figure 62. Breakdown of Annual 8S Operational Costs Based on 500 Annual Flight Hours

As it can be clearly seen above, a major part of the total operational cost emanates from the annual fuel cost followed in second by the crew cost. Therefore, the individual costs can be counteracted by increasing the flight hours that the airplane flies in a year. The current operational parameter was chosen as 500 flight hours annually, which is reasonable. This value can range from 100 to 1500 flight hours in such business jets which presents a large volume of movement for the Coronis aircraft to balance the total operational costs with the profit made from various utilizations of the airplane. The Coronis designers expect this airplane to more realistically fly around 1000 flight hours a year due to the high accessibility and versatility that this aircraft has with respect to the sheer amount of short and soft/dirt airstrips available

for this design. For example, the medical and utility layouts promise to fulfill this design mission through the utilization of Coronis as air ambulance or cargo/bush plane in relatively inaccessible locations around the world, primarily in South America and sub-Saharan Africa.

With the given operational cost model, the cost to fly the Coronis for an hour is around \$1,300 which is on the less expensive side when compared to light business jets of similar size, configuration, and mission. This can be seen in Table XXXVIII below which clearly demonstrates the economical superiority of Coronis with respect to other aircraft in terms of cost per flight hour [16].

Table XXXVIII. Comparison of the operational cost to various aircraft of similar type.

Aircraft Name	Cost Per Flight Hour
Coronis 8	\$1,300
Cessna Citation M2	\$1,395
SyberJet SJ30	\$1,608
Nextant Aerospace XTi	\$1,623
Cessna Citation CJ3+	\$1,680
Embraer Phenom 300	\$1,758

15. Aircraft Dimensions

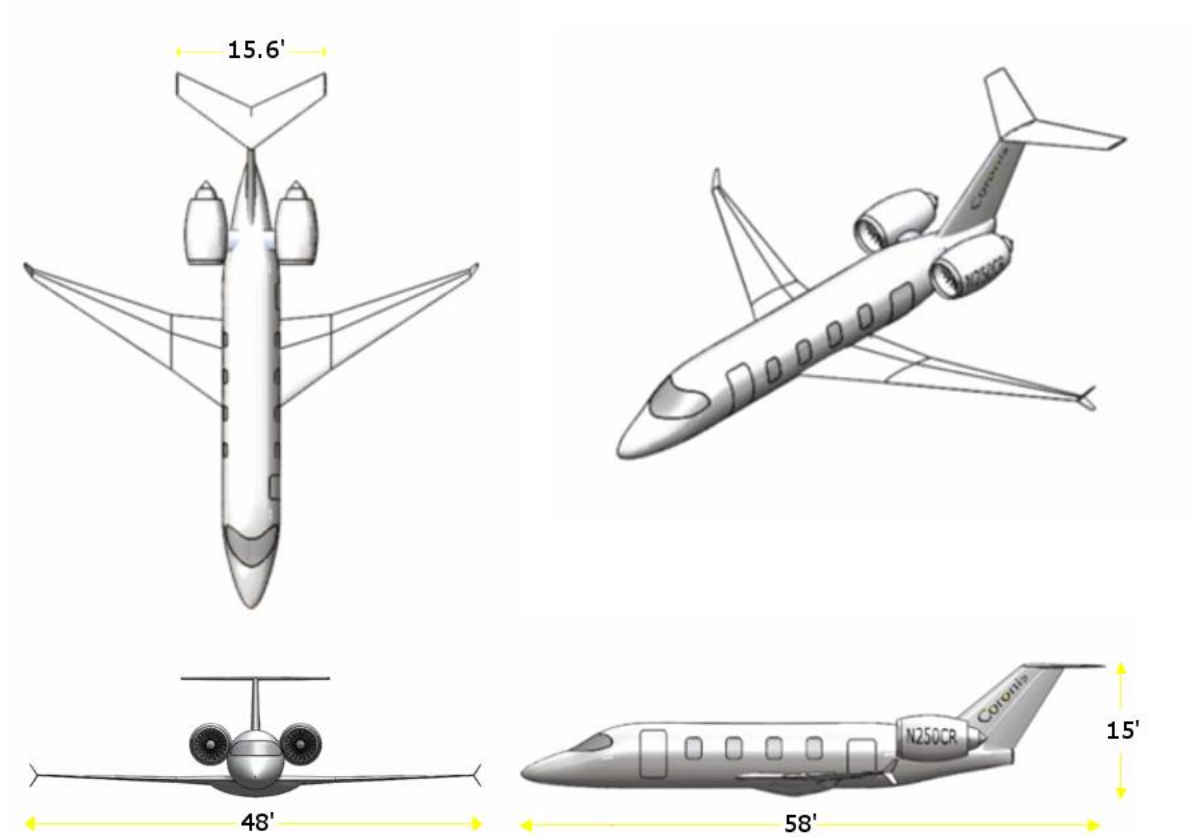


Figure 63. Coronis 8S Dimensions

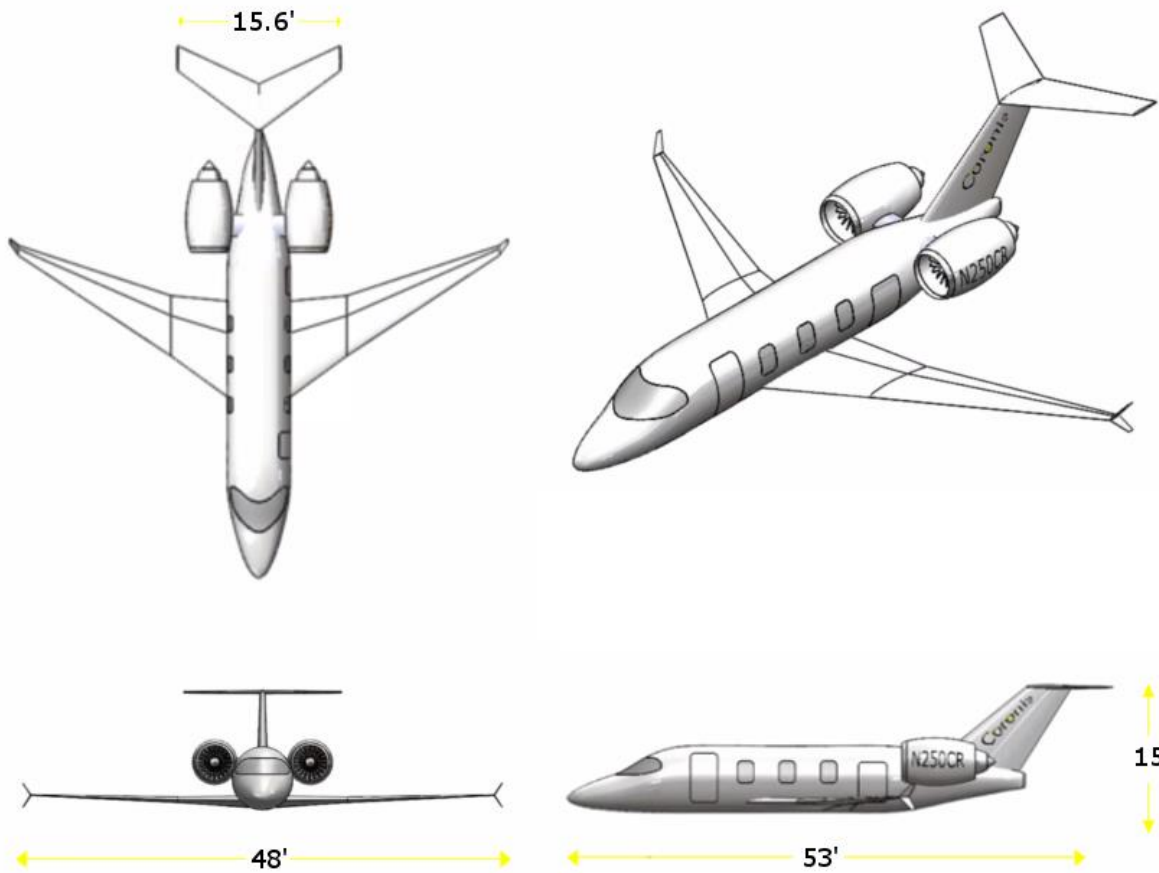


Figure 64. Coronis 6S Dimensions

Bibliography

- [1] United States Department of Transportation, "Table 1-3: Number of U.S. Airports," 31 August 2015. [Online]. Available: https://www.rita.dot.gov/bts/sites/rita.dot.gov.bts/files/publications/national_transportation_statistics/html/table_01_03.html. [Accessed 26 April 2017].
- [2] D. J. Roskam, Airplane Design Part I: Preliminary Sizing of Airplanes., Lawrence: DARcorporation, 2005.
- [3] D. J. Roskam, Airplane Design Part II: Preliminary Configuration Design and Integration of the Propulsion System, Lawrence: DARcorporation, 2004.
- [4] D. J. Roskam, Airplane Design Part V: Component Weight Estimation, Ottawa, Kansas: Roskam Aviation and Engineering Corporation, 1985.
- [5] Safran Nacelles, "Nacelle systems for business jets," [Online]. Available: <https://www.safran-nacelles.com/nacelle-systems/nacelle-systems-business-jets/cessna-citation-longituder-thrust-reversers>.
- [6] European Aviation Safety Agency, "EASA Type-Certificate Data Sheet TFE731-20, -40, -50, -60 series engines," 2013.
- [7] Honeywell Aerospace, "TFE731 Turbofan Engine," [Online]. Available: <https://aerospace.honeywell.com/en/products/engines/tfe731-turbofan-engine>.
- [8] N. Meier, "Civil Turbojet/Turbofan Specifications," 3 April 2005. [Online]. Available: <http://www.jet-engine.net/civtfspec.html>.
- [9] Honeywell Aerospace, "RE100 APU for Citation Sovereign and XLS," Phoenix, 2006.
- [10] Honeywell Aerospace, "RE100 Auxiliary Power Unit for Learjet 45," Phoenix, 2009.
- [11] Cessna Aircraft Company, "Specification and Description, Cessna Citation XLS+," Wichita, 2014.
- [12] H. D. Mattingly, Aircraft Engine Design, Washington: AIAA, 1987.
- [13] R. C. Nelson, Flight Stability and Automatic Control, New Delhi: McGraw Hill Education (India) Private Limited, 2007.
- [14] D. J. Roskam, Airplane Design Part III: Layout Design of Cockpit, Fuselage, Wing and Empennage, Lawrence: DARcorporation, 1986.
- [15] S. Gudmundsson, General Aviation Aircraft Design, Oxford, UK: Elsevier Inc., 2014.
- [16] A. K. Marsh, "AOPA," 16 November 2015. [Online]. Available: <https://www.aopa.org/news-and-media/all-news/2015/november/16/hourly-operating-costs-of-45-jets-compared>. [Accessed 26 April 2016].